JℲM PAPERS

Composition of resolvents enhanced by random sweeping for large-scale structures in turbulent channel flows

Ting Wu[1,2] **and Guowei He**[1,2],†

[1]The State Key Laboratory of Nonlinear Mechanics, Institute of Mechanics, Chinese Academy of Sciences, Beijing 100190, PR China

[2]School of Engineering Sciences, University of Chinese Academy of Sciences, Beijing 100049, PR China

Composite sweeping-enhanced resolvents, referred to as the R_s^2 model, are proposed to predict the space–time statistics of large-scale structures in turbulent channel flows. This model incorporates two key mechanisms: (i) eddy damping is introduced to represent random sweeping decorrelation caused by nonlinear forcing, leading to a sweeping-enhanced resolvent R_s; and (ii) the sweeping-enhanced resolvent R_s is composited into its iterations R_s^2 to yield non-zero Taylor time microscales. The resulting R_s^2 model can correctly predict the frequency spectra and two-point cross-spectra of large-scale structures. This model is compared numerically with eddy-viscosity-enhanced resolvent models. The latter are designed to represent energy transfer instead for time decorrelation, and thus underpredict the characteristic decay time scales. The R_s^2 model correctly yields the characteristic decay time scales in turbulent channel flows.

Key words: turbulence modelling, turbulent boundary layers

1. Introduction

Resolvent analysis (McKeon & Sharma 2010; McKeon 2017) is increasingly used to study the space–time properties of large-scale structures in turbulent shear flows. In this analysis, the Navier–Stokes (NS) equations are represented as the sum of a linear part and nonlinear terms, where the linear part is treated as a resolvent operator, and the nonlinear terms are treated as nonlinear forcing. In input–output analysis (Jovanović 2021), the nonlinear forcing acts as the input to generate velocity fluctuations that are output through the resolvent. Therefore, the modelling of nonlinear forcing essentially determines the space–time properties of turbulent fluctuations. The present paper addresses the modelling

† Email address for correspondence: hgw@lnm.imech.ac.cn

of nonlinear forcing for predicting the frequency spectra and two-point cross-spectra of large-scale structures in wall-bounded turbulent flows.

Nonlinear forcing is usually treated as white noise in the linearized NS equations (LNSEs) and the resolvent-based methods. White-in-time random forcing (Farrell & Ioannou 1993), white-in-space random forcing (Semeraro *et al.* 2016; Schmidt *et al.* 2018; Lesshafft *et al.* 2019) and random forcing that is white in both time and space (Farrell & Ioannou 1998; Bamieh & Dahleh 2001; Jovanović & Bamieh 2005) have been applied to study the space–time properties of coherent structures in turbulent flows. In particular, Liu & Gayme (2020) used white-in-time random forcing to calculate the space–time energy spectra and convection velocities in turbulent channel flows. The obtained convection velocities tend to approach a constant value near the wall and are in good agreement with the direct numerical simulations (DNS) results (Geng *et al.* 2015). However, it has been shown (Wu & He 2021*a,b*) that white-in-time random forcing acting directly on velocity fluctuations leads to vanishing Taylor time microscales and thus divergent bandwidths of frequency spectra at fixed wavenumbers, which is inconsistent with the physics of turbulent flows.

Nonlinear forcing is found to be coloured in both space and time (Towne, Brès & Lele 2017; Morra *et al.* 2021; Nogueira *et al.* 2021; Karban *et al.* 2022). Nogueira *et al.* (2021) demonstrated that nonlinear forcing in turbulent Couette flows exhibits coherent structures such as a streamwise vortex. Morra *et al.* (2021) showed that nonlinear forcing in turbulent channel flows is coloured in time and coherent in space. The coherence of nonlinear forcing implies that coloured random forcing is necessarily introduced to correctly predict the space–time statistics of turbulence (Moarref *et al.* 2014; Rosenberg, Symon & McKeon 2019; Martini *et al.* 2020; McMullen, Rosenberg & McKeon 2020; Towne, Lozano-Durán & Yang 2020; Yang *et al.* 2020). Recently, Zare, Jovanović & Georgiou (2017) and Zare, Georgiou & Jovanović (2020) showed that white-in-time forcing cannot reproduce the spatial cross-spectra in turbulent channel flows. Therefore, they proposed that nonlinear forcing is the sum of white-in-time forcing and dynamic filtering of white-in-time forcing. The obtained nonlinear forcing is equivalent to a modified linearized NS operator with white-in-time forcing (Zare *et al.* 2017).

To account for the spatiotemporal coherence of nonlinear forcing, eddy-viscosity-enhanced random forcing is introduced in the LNSEs and resolvent analysis (Hwang & Cossu 2010*a,b*; Moarref & Jovanović 2012; Illingworth, Monty & Marusic 2018; Pickering *et al.* 2021; Ran, Zare & Jovanović 2021; Symon, Illingworth & Marusic 2021). The random forcing is assumed to be the sum of the eddy viscosity term and the white noise, where the Cess model (Cess 1958; Reynolds & Hussain 1972) is used for the eddy viscosity. Hwang & Cossu (2010*a,b*) used eddy-viscosity-enhanced LNSEs to investigate energy amplification in turbulent Couette flows and turbulent channel flows. The obtained optimal spanwise wavenumbers are in good agreement with the characteristic length scales of the streaks observed in experiments and numerical simulations. Morra *et al.* (2019) used eddy-viscosity-enhanced random forcing to estimate the space–time energy spectrum and cross-spectrum of buffer-layer structures and large-scale structures in turbulent channel flows. Their results are superior to those obtained from white forcing because the projection of eddy-viscosity-enhanced forcing onto resolvent modes is similar to the projection of DNS forcing onto the same resolvent modes (Morra *et al.* 2021). Pickering *et al.* (2021) used a data-driven approach to determine the optimal eddy viscosity in a turbulent jet by maximizing the projection of the dominant resolvent modes onto the leading spectral proper orthogonal decomposition (SPOD) modes. This approach significantly improved the consistency between the resolvent modes

and SPOD modes. Gupta *et al.* (2021) proposed that the eddy viscosity and forcing intensity depend on the wavelengths and wall distances. The wavelength dependence of the eddy viscosity causes the small-wavelength fluctuations to not be overdamped, while the wall-distance dependence of the forcing intensity leads to a wall-normal distribution of energy production similar to that of the DNS result. As a result, their model can predict the large-scale velocity fluctuations at several wall-normal locations from the measurements at a single wall-normal location in the logarithmic region. In the present paper, we introduce sweeping-enhanced random forcing to predict the frequency spectra and two-point cross-spectra of large-scale structures.

The sweeping-enhanced random forcing is built on the random sweeping hypothesis in homogeneous isotropic turbulence. Kraichnan (1964) and Tennekes (1975) assumed that the inertial-scale eddies are swept past the Eulerian observation point by the energy-containing eddies, thus the time correlations of Eulerian velocities are determined by the sweeping velocities (Kraichnan 1964; He, Jin & Yang 2017). The sweeping velocities are defined as the root mean square (r.m.s.) of velocity fluctuations, giving the decorrelation time scales of the velocity modes and thus the bandwidths of the frequency spectra. Consequently, the sweeping velocities can be used to determine the time scales of random forcing.

Recently, the dynamic autoregressive (DAR) model has been developed to predict the space–time energy spectra in turbulent channel flows (Wu & He 2021*b*). Two techniques are introduced in the DAR model.

First, eddy damping is introduced to represent the random sweeping effect in nonlinear forcing. It is well-known that this effect dominates the decorrelation process and consequently the frequency spectra at fixed wavenumbers not only in homogeneous isotropic turbulence but also in turbulent channel flows (Kraichnan 1964; Tennekes 1975; He & Zhang 2006; Zhao & He 2009; Wilczek & Narita 2012; He *et al.* 2017). The decorrelation time scales characterize the decay rates of the time correlations and determine the spectral broadening of the space–time energy spectrum, which is crucial to estimate the power fluctuations in wind farms (Bossuyt, Meneveau & Meyers 2017), turbulence noise (Rubinstein & Zhou 1999, 2000; He, Wang & Lele 2004) and wall-pressure spectra (Slama, Leblond & Sagaut 2018). Therefore, the random sweeping effect should be taken into account, leading to a sweeping-enhanced resolvent, while the remaining effect in nonlinear forcing is modelled by random forcing. Second, random forcing is generated using dynamic regression. That is, the random forcing is the mapping from the input noise, which is then mapped to the output response. Therefore, the output response is the double mapping of input noise, thus no white-in-time random forcing acts directly on the output response. Therefore, the DAR model can reproduce the space–time statistics at a given wall-normal location. However, it cannot reproduce the cross-spectra between two different wall-normal locations since the linear part of the DAR model includes only the convection term and excludes the moment transfer in the wall-normal direction. In this paper, we use a resolvent operator to replace the linear part of the DAR model to account for the moment transfer in the wall-normal direction.

The present work is developed by analogy to the DAR model in the resolvent framework. Sweeping-enhanced random forcing is introduced to construct the sweeping-enhanced resolvent operator. The random sweeping effects in the streamwise–spanwise plane and the wall-normal direction are considered separately. The composite sweeping-enhanced resolvent operator is proposed to generate space–time coherent random forcing so as to reproduce correctly the frequency spectra of large-scale structures. The remainder of this paper is organized as follows. The DAR model is presented briefly in §2 to better

understand the composite sweeping-enhanced resolvent. In § 3, the sweeping-enhanced resolvent is introduced first, then the composite resolvent operators are presented. Then this new proposed model is compared with the variants of the eddy-viscosity-enhanced resolvent models. Both sweeping-enhanced and eddy-viscosity-enhanced resolvent models are investigated by using DNS of turbulent channel flows in § 4. Conclusions and future work are given in § 5.

2. Composition of the transfer functions for the DAR model

In this section, the DAR model is rewritten as the composition of the sweeping-enhanced transfer functions. We use the term 'transfer function' to denote the map from an input to an output in the framework of the DAR model. The term 'transfer function' is replaced by the term 'resolvent' or 'resolvent operator' in resolvent analysis to denote the map from random forcing to responses.

Consider the streamwise velocity fluctuation $u(x, z, t, y)$ and its spatial Fourier mode $\hat{u}(\mathbf{k}, t, y)$ at a given wall-normal location y in the channel. In this paper, $\hat{\cdot}$ denotes the spatial Fourier mode, $\tilde{\cdot}$ denotes the space–time Fourier mode, x, y and z represent the streamwise, wall-normal and spanwise coordinates, respectively, t denotes time, and $\mathbf{k} = (k_x, k_z)$ is the wavenumber vector, where k_x and k_z are the streamwise and spanwise wavenumbers, respectively. In this section, only a single wall-normal location y is considered, thus for convenience, y in the independent variables is not expressed explicitly.

The DAR model is written as (Wu & He 2021*a*,*b*)

$$\partial_t \hat{u} = -\mathrm{i}k_x U_c \hat{u} + \hat{F}, \tag{2.1}$$

$$\partial_t \hat{F} = -\mathrm{i}k_x U_c \hat{F} - (k_x^2 V_x^2 + k_z^2 V_z^2)\hat{u} - 2\sqrt{k_x^2 V_x^2 + k_z^2 V_z^2}\,\hat{F} + \hat{f}_t, \tag{2.2}$$

where U_c is the convection velocity, and V_x and V_z represent the streamwise and spanwise sweeping velocities, respectively. The convection velocity is the speed of downstream movement of eddies that can be determined by the first-order moments of space–time energy spectra, and is usually approximated by the mean velocity. The sweeping velocity is the variation velocity of eddies that can be determined by the second-order moments of space–time energy spectra, and is usually approximated by the r.m.s. of velocity fluctuations. The original random forcing $\hat{f}_t$ in (2.2) is given by $\hat{f}_t = \sqrt{2(k_x^2 V_x^2 + k_z^2 V_z^2)^{3/2} \Phi(\mathbf{k})}\,\hat{\xi}(\mathbf{k}, t)$, where $\hat{\xi}(\mathbf{k}, t)$ is the white-in-time noise that satisfies $\langle \hat{\xi}^*(\mathbf{k}, t)\hat{\xi}(\mathbf{k}', t') \rangle = 2\,\delta(\mathbf{k} - \mathbf{k}')\,\delta(t - t')$, with δ being the Dirac delta function, and where $\Phi(\mathbf{k})$ is the spatial energy spectrum.

The velocity mode $\hat{u}$ is governed by the convection term $-\mathrm{i}k_x U_c \hat{u}$ and the total random forcing $\hat{F}$. The forcing $\hat{F}$ represents the distortion that causes the decorrelation of velocity fluctuations, and is determined by convection $-\mathrm{i}k_x U_c \hat{F}$, sweeping $-(k_x^2 V_x^2 + k_z^2 V_z^2)\hat{u}$, damping $-2\sqrt{k_x^2 V_x^2 + k_z^2 V_z^2}\,\hat{F}$ and original random forcing $\hat{f}_t$. Note that both the sweeping $-(k_x^2 V_x^2 + k_z^2 V_z^2)\hat{u}$ and the damping $-2\sqrt{k_x^2 V_x^2 + k_z^2 V_z^2}\,\hat{F}$ in (2.2) result from the random sweeping velocities. Therefore, the DAR model can predict the space–time energy spectrum at a given wall-normal location from the spatial energy spectrum.

We introduce the intermediate random forcing $\hat{f}$ as an intermediate variable, and write the total random forcing $\hat{F}$ as

$$\hat{F} = -\sqrt{k_x^2 V_x^2 + k_z^2 V_z^2}\,\hat{u} + \hat{f}. \tag{2.3}$$

Then the DAR model is rewritten as

$$\partial_t \hat{u} = -\mathrm{i}k_x U_c \hat{u} - \sqrt{k_x^2 V_x^2 + k_z^2 V_z^2}\,\hat{u} + \hat{f}, \qquad (2.4)$$

$$\partial_t \hat{f} = -\mathrm{i}k_x U_c \hat{f} - \sqrt{k_x^2 V_x^2 + k_z^2 V_z^2}\,\hat{f} + \hat{f}_t. \qquad (2.5)$$

Taking the temporal Fourier transform of (2.4) and (2.5), we obtain

$$\tilde{u} = R_s \tilde{f}, \qquad (2.6)$$

$$\tilde{f} = R_s \tilde{f}_t. \qquad (2.7)$$

Here, $\tilde{\cdot}$ denotes the space–time Fourier mode, and R_s is the sweeping-enhanced transfer function given by

$$R_s = \left(-\mathrm{i}\omega + \mathrm{i}k_x U_c + \sqrt{k_x^2 V_x^2 + k_z^2 V_z^2}\right)^{-1}, \qquad (2.8)$$

where ω is the frequency. Hence the DAR model can be written as

$$\tilde{u} = R_s^2 \tilde{f}_t. \qquad (2.9)$$

In (2.6), R_s is the transfer function from the input $\tilde{f}$ to the output $\tilde{u}$. In (2.7), R_s is also the transfer function from the input $\tilde{f}_t$ to the output $\tilde{f}$. According to (2.9), if we take $\tilde{f}_t$ as the input and $\tilde{u}$ as the output, then the transfer function is the composition of two transfer functions, R_s^2.

We calculate the spatial spectrum of $\hat{F}$ as follows:

$$\langle |\hat{F}|^2 \rangle = (k_x^2 V_x^2 + k_z^2 V_z^2)\langle |\hat{u}|^2 \rangle + \langle |\hat{f}|^2 \rangle - 2\sqrt{k_x^2 V_x^2 + k_z^2 V_z^2}\,\mathrm{Re}\langle \hat{u}\hat{f}^* \rangle, \qquad (2.10)$$

where $\langle \cdot \rangle$ represents the ensemble average. Therefore,

$$\langle |\hat{f}|^2 \rangle = \int \langle |\tilde{f}|^2 \rangle \, \mathrm{d}\omega = \int |R_s|^2 \langle |\tilde{f}_t|^2 \rangle \, \mathrm{d}\omega, \qquad (2.11)$$

$$\langle |\hat{u}|^2 \rangle = \int \langle |\tilde{u}|^2 \rangle \, \mathrm{d}\omega = \int |R_s|^4 \langle |\tilde{f}_t|^2 \rangle \, \mathrm{d}\omega \qquad (2.12)$$

and

$$\langle \hat{u}\hat{f}^* \rangle = \int \langle \tilde{u}\tilde{f}^* \rangle \, \mathrm{d}\omega = \int R_s^2 R_s^* \langle |\tilde{f}_t|^2 \rangle \, \mathrm{d}\omega. \qquad (2.13)$$

Noting that $\tilde{f}_t$ is white-in-time, we have

$$\frac{\langle |\hat{f}|^2 \rangle}{\mathrm{Re}\langle \hat{u}\hat{f}^* \rangle} = \frac{\displaystyle\int |R_s|^2 \, \mathrm{d}\omega}{\displaystyle\int \mathrm{Re}(R_s^2 R_s^*) \, \mathrm{d}\omega} = 2\sqrt{k_x^2 V_x^2 + k_z^2 V_z^2} \qquad (2.14)$$

and

$$\frac{\langle |\hat{f}|^2 \rangle}{\langle |\hat{u}|^2 \rangle} = \frac{\displaystyle\int |R_s|^2 \, \mathrm{d}\omega}{\displaystyle\int |R_s|^4 \, \mathrm{d}\omega} = 2(k_x^2 V_x^2 + k_z^2 V_z^2). \qquad (2.15)$$

The substitution of (2.14) into (2.10) gives

$$\langle|\hat{F}|^2\rangle = (k_x^2 V_x^2 + k_z^2 V_z^2)\langle|\hat{u}|^2\rangle, \tag{2.16}$$

showing that the spatial spectrum of the total random forcing $\hat{F}$ is equal to that of the sweeping term $-\sqrt{k_x^2 V_x^2 + k_z^2 V_z^2}\,\hat{u}$.

The new expressions (2.6) and (2.7) for the DAR model suggest two techniques for resolvent analysis to reproduce the desired Taylor time microscales. The first is the use of the sweeping-enhanced transfer function, as defined by (2.8). It can be seen from (2.3) that the sweeping term $-\sqrt{k_x^2 V_x^2 + k_z^2 V_z^2}\,\hat{u}$ causes temporal decorrelation. Therefore, if the velocity mode is dominated by the sweeping term, then the characteristic decorrelation time scale is inversely proportional to the sweeping coefficient $\sqrt{k_x^2 V_x^2 + k_z^2 V_z^2}$, which is consistent with the random sweeping model (Kraichnan 1964; Tennekes 1975; Wilczek, Stevens & Meneveau 2015*b*). Therefore, it is reasonable to introduce the sweeping term into the resolvent analysis. The second technique is the use of composite transfer functions, as expressed in (2.9). In resolvent analysis, only one transfer function is used to map white-in-time random forcing to its response, leading to the vanishing Taylor time microscale of the response. In the DAR model, two transfer functions are used: the first maps white-in-time random forcing to a coloured random forcing of finite correlation time scales, and the second maps the coloured random forcing to the response of the desired correlation time scales. In this way, the composition of the two transfer functions is introduced rationally into resolvent analysis.

The DAR model can predict the space–time energy spectra at a single wall-normal location. However, the DAR model cannot reproduce the space–time cross-spectra between two wall-normal locations because it contains only the mean velocity convection at a fixed wall-normal location without any coupling between different wall-normal locations. One solution to this problem is to replace the convection term with the LNSEs in the resolvent analysis to reproduce the two-point cross-spectra. In the next section, the resolvent operator enhanced by the sweeping velocities is introduced for space–time cross-spectra.

3. Composition of the sweeping-enhanced resolvents

In this section, composite resolvent analysis is developed for space–time spectra, such as the frequency spectra and the two-point cross-spectra of large-scale structures. The sweeping-enhanced resolvent is introduced in § 3.1, and is compared with the eddy-viscosity-enhanced resolvent in § 3.3. The composite resolvents are presented in § 3.2.

3.1. *Sweeping-enhanced resolvent*

We first rewrite the governing equations for the fluctuations in the following form for resolvent analysis:

$$\partial_t \boldsymbol{u} + (\boldsymbol{u} \cdot \nabla)\boldsymbol{U} + (\boldsymbol{U} \cdot \nabla)\boldsymbol{u} + \nabla p - \nu \nabla^2 \boldsymbol{u} = -(\boldsymbol{u} \cdot \nabla)\boldsymbol{u} + \langle(\boldsymbol{u} \cdot \nabla)\boldsymbol{u}\rangle \equiv \boldsymbol{F}, \tag{3.1}$$

$$\nabla \cdot \boldsymbol{u} = 0, \tag{3.2}$$

where $\boldsymbol{u} = [u, v, w]^{\mathrm{T}}$, with u, v and w the velocity fluctuations in the streamwise, wall-normal and spanwise directions, respectively, $\boldsymbol{U}$ is the mean velocity, p is the pressure

956 A31-6

fluctuation, and ν is the kinematic viscosity. Here, F arises from the nonlinear term in the NS equations that is treated as nonlinear forcing in the resolvent analysis.

Taking the spatial (x–z) Fourier transform of (3.1) and (3.2), we obtain

$$\frac{\partial}{\partial t} \begin{bmatrix} I & \\ & 0 \end{bmatrix} \hat{q} = \begin{bmatrix} L & -\hat{\nabla} \\ -\hat{\nabla}^{\mathrm{T}} & 0 \end{bmatrix} \hat{q} + B\hat{F}, \tag{3.3}$$

where $\hat{q} = [\hat{u}, \hat{v}, \hat{w}, \hat{p}]^{\mathrm{T}}$, $\hat{\nabla} = [\mathrm{i}k_x, \partial_y, \mathrm{i}k_z]^{\mathrm{T}}$, I is the 3×3 identity matrix, and the operators L and B are

$$L = \begin{bmatrix} -\mathrm{i}k_x U + \nu \hat{\nabla}^2 & -U' & 0 \\ 0 & -\mathrm{i}k_x U + \nu \hat{\nabla}^2 & 0 \\ 0 & 0 & -\mathrm{i}k_x U + \nu \hat{\nabla}^2 \end{bmatrix}, \tag{3.4}$$

$$B = \begin{bmatrix} I \\ 0 \end{bmatrix}, \tag{3.5}$$

with U' the mean shear. In this paper, a prime indicates the wall-normal derivative.

Taking the temporal Fourier transform of (3.3), we obtain

$$\tilde{u} = R\tilde{F}, \tag{3.6}$$

where R is the resolvent that is given by

$$R = B^{\mathrm{T}} \left(-\mathrm{i}\omega \begin{bmatrix} I & \\ & 0 \end{bmatrix} - \begin{bmatrix} L & -\hat{\nabla} \\ -\hat{\nabla}^{\mathrm{T}} & 0 \end{bmatrix} \right)^{-1} B. \tag{3.7}$$

By analogy to the random forcing in (2.3) for the DAR model, the nonlinear forcing $\hat{F}$ in (3.3) is modelled as

$$\hat{F} = -\sqrt{k_x^2 V_x^2(y) + k_z^2 V_z^2(y)}\, \hat{u} + \lambda_y(k, y)\, \partial_y \left(V_y(y)\, \partial_y \right) \hat{u} + \hat{f}, \tag{3.8}$$

where $V_x(y)$, $V_y(y)$ and $V_z(y)$ are the sweeping velocities in the streamwise, wall-normal and spanwise directions, respectively, and $\lambda_y(k, y)$ is the characteristic length scale in the wall-normal direction.

The first two terms on the right-hand side of (3.8) represent the eddy damping caused by the random sweeping effect, and the third term, $\hat{f}$, represents the remaining effects of nonlinear forcing. Note that the first term, which is the same as that in (2.3) for the DAR model, represents the random sweeping in the x–z plane caused by the streamwise and spanwise motions of energetic eddies. The second term is in the form of wall-normal dissipation and represents the random sweeping in the wall-normal direction caused by the wall-normal motion of energetic eddies. This dissipation term is determined by the characteristic length scale $\lambda_y(k, y)$ and the random sweeping velocity $V_y(y)$ that is associated with wall-normal velocities. The wall-normal dissipation term increases the wall-normal correlations of turbulent structures. In the present study, the sweeping velocities are taken as the r.m.s. of velocity fluctuations, i.e. $V_x(y) = \sqrt{\langle u^2(y) \rangle}$, $V_y(y) = \sqrt{\langle v^2(y) \rangle}$ and $V_z(y) = \sqrt{\langle w^2(y) \rangle}$. The sweeping velocities depend on the wall-normal location. In particular, in the logarithmic region, the sweeping velocities decrease with increasing wall distance, leading to a slower decay of the time correlations. This is consistent with the physics of turbulent channel flows. However, it cannot be achieved

by the eddy viscosity because the eddy viscosity in the logarithmic region increases with increasing wall distance (see the discussion in § 3.3).

In the DAR model, we consider the space–time energy spectra at only one wall-normal location, and ignore the momentum exchange in the wall-normal direction. Consequently, the DAR model cannot yield the cross-spectra between two wall-normal locations. To account for the momentum exchange in the wall-normal direction, the second term on the right-hand side of (3.8) is introduced, where the wall-normal sweeping velocity V_y and the characteristic length scale $\lambda_y(\boldsymbol{k}, y)$ are used.

Next, we explain how to determine the characteristic length scale $\lambda_y(\boldsymbol{k}, y)$.

First, we estimate the spatial spectra of nonlinear forcing. The nonlinear forcing $\boldsymbol{F}_{xz}$ caused by the streamwise and spanwise velocity fluctuations is given by

$$\boldsymbol{F}_{xz} \equiv -u \, \partial_x \boldsymbol{u} - w \, \partial_z \boldsymbol{u} + \langle u \, \partial_x \boldsymbol{u} + w \, \partial_z \boldsymbol{u} \rangle. \tag{3.9}$$

Meanwhile, the nonlinear forcing $\boldsymbol{F}_y$ caused by the wall-normal velocity fluctuations is given by

$$\boldsymbol{F}_y \equiv -v \, \partial_y \boldsymbol{u} + \langle v \, \partial_y \boldsymbol{u} \rangle. \tag{3.10}$$

According to the random sweeping hypothesis, u, v and w in (3.9) and (3.10) can be represented by the random sweeping velocities v_x, v_y and v_z, respectively, where the random sweeping velocities are considered to be constant in space. As a result, for the non-zero wavenumber vectors, the random sweeping hypothesis leads to

$$\hat{\boldsymbol{F}}_{xz} \sim -\mathrm{i}k_x v_x \hat{\boldsymbol{u}} - \mathrm{i}k_z v_z \hat{\boldsymbol{u}} \tag{3.11}$$

and

$$\hat{\boldsymbol{F}}_y \sim -v_y \, \partial_y \hat{\boldsymbol{u}}. \tag{3.12}$$

The random sweeping velocities are usually assumed to be independent of $\hat{\boldsymbol{u}}$, leading to the spatial spectra of nonlinear forcing

$$\langle |\hat{\boldsymbol{F}}_{xz}(\boldsymbol{k}, y)|^2 \rangle = [k_x^2 \, V_x^2(y) + k_z^2 \, V_z^2(y)] \langle |\hat{\boldsymbol{u}}|^2 \rangle \tag{3.13}$$

and

$$\langle |\hat{\boldsymbol{F}}_y(\boldsymbol{k}, y)|^2 \rangle = V_y^2(y) \, \langle |\partial_y \hat{\boldsymbol{u}}|^2 \rangle, \tag{3.14}$$

where $V_x^2 = \langle v_x^2 \rangle$, $V_y^2 = \langle v_y^2 \rangle$ and $V_z^2 = \langle v_z^2 \rangle$.

Second, we estimate the spatial spectra of eddy damping. In (3.8), the eddy damping caused by the streamwise and spanwise velocity fluctuations is

$$\hat{\boldsymbol{F}}_{xz}^d(\boldsymbol{k}, y) = -\sqrt{k_x^2 \, V_x^2(y) + k_z^2 \, V_z^2(y)} \, \hat{\boldsymbol{u}}, \tag{3.15}$$

and the eddy damping caused by the wall-normal velocity fluctuations is

$$\hat{\boldsymbol{F}}_y^d(\boldsymbol{k}, y) = \lambda_y(\boldsymbol{k}, y) \, \partial_y(V_y(y) \, \partial_y) \, \hat{\boldsymbol{u}}. \tag{3.16}$$

Thus we obtain the spatial spectra of eddy damping:

$$\langle |\hat{\boldsymbol{F}}_{xz}^d(\boldsymbol{k}, y)|^2 \rangle = [k_x^2 \, V_x^2(y) + k_z^2 \, V_z^2(y)] \, \langle |\hat{\boldsymbol{u}}|^2 \rangle \tag{3.17}$$

and

$$\langle |\hat{\boldsymbol{F}}_y^d(\boldsymbol{k}, y)|^2 \rangle = \lambda_y^2(\boldsymbol{k}, y) \, \langle |\partial_y(V_y(y) \, \partial_y) \, \hat{\boldsymbol{u}}|^2 \rangle. \tag{3.18}$$

Third, we match the spatial spectra of eddy damping with nonlinear forcing. It can be seen that

$$\langle |\hat{\boldsymbol{F}}^d_{xz}(\boldsymbol{k}, y)|^2 \rangle = \langle |\hat{\boldsymbol{F}}_{xz}(\boldsymbol{k}, y)|^2 \rangle. \tag{3.19}$$

That is, the spatial spectra of the eddy damping caused by the streamwise and spanwise velocity fluctuations are equal to the spatial spectra of nonlinear forcing $\boldsymbol{F}_{xz}$ caused by the streamwise and spanwise velocity fluctuations, which is similar to (2.16) in the DAR model. Consistently, we require $\langle |\hat{\boldsymbol{F}}^d_y(\boldsymbol{k}, y)|^2 \rangle = \langle |\hat{\boldsymbol{F}}_y(\boldsymbol{k}, y)|^2 \rangle$ – that is, the spatial spectra of the eddy damping caused by the wall-normal velocity fluctuations are equal to those of nonlinear forcing $\boldsymbol{F}_y$ caused by the wall-normal velocity fluctuations. Therefore, we obtain

$$\lambda_y(\boldsymbol{k}, y) = \sqrt{\frac{V_y^2(y) \langle |\partial_y \hat{\boldsymbol{u}}|^2 \rangle}{\langle |\partial_y (V_y(y) \partial_y) \hat{\boldsymbol{u}}|^2 \rangle}}. \tag{3.20}$$

Figure 1 shows $\lambda_y(\boldsymbol{k}, y)$ for the turbulent channel flows at $Re_\tau = 180$ and 550, where the wavenumber vector $\boldsymbol{k}h = (2, 4)$ represents large-scale structures, and $Re_\tau = u_\tau h/\nu$ is the Reynolds number based on the friction velocity u_τ, with h being the half-height of the channel. We use the semicircle function to fit the wall-normal distribution of $\lambda_y(\boldsymbol{k}, y)$:

$$\lambda_y(\boldsymbol{k}, y) = \beta(\boldsymbol{k}) \sqrt{h^2 - y^2}, \tag{3.21}$$

where $\beta(\boldsymbol{k})$ is determined to minimize the error $\int_{-h}^{h} [\lambda_y^{DNS}(\boldsymbol{k}, y) - \beta(\boldsymbol{k})\sqrt{h^2 - y^2}]^2 \, \mathrm{d}y$. That is,

$$\beta(\boldsymbol{k}) = \frac{\displaystyle\int_{-h}^{h} \lambda_y^{DNS}(\boldsymbol{k}, y) \sqrt{h^2 - y^2} \, \mathrm{d}y}{\displaystyle\int_{-h}^{h} (h^2 - y^2) \, \mathrm{d}y}, \tag{3.22}$$

where $\lambda_y^{DNS}(\boldsymbol{k}, y)$ is the result obtained from (3.20) through DNS data. For the wavenumber vector $\boldsymbol{k}h = (2, 4)$, $\beta(\boldsymbol{k}) = 0.075$ at $Re_\tau = 180$, and $\beta(\boldsymbol{k}) = 0.046$ at $Re_\tau = 550$. In this paper, $\beta(\boldsymbol{k})$ is determined from (3.22) using DNS data. The numerical examination shows that the results are not sensitive to the parameter $\lambda_y(\boldsymbol{k}, y)$. In fact, the constant $\lambda_y(\boldsymbol{k}, y) = 0.045h$ leads to results similar to those obtained from (3.21) and (3.22).

Finally, we substitute the model (3.8) for nonlinear forcing into the governing equation (3.3) for resolvent analysis, and take the temporal Fourier transform of the resultant equation, giving the space–time Fourier mode $\tilde{\boldsymbol{u}}$ of velocity fluctuation as

$$\tilde{\boldsymbol{u}} = \boldsymbol{R}_s \tilde{\boldsymbol{f}}. \tag{3.23}$$

The operator $\boldsymbol{R}_s$ is given by

$$\boldsymbol{R}_s = \boldsymbol{B}^{\mathrm{T}} \left(-\mathrm{i}\omega \begin{bmatrix} \boldsymbol{I} \\ \boldsymbol{0} \end{bmatrix} - \begin{bmatrix} \boldsymbol{L}_s & -\hat{\boldsymbol{\nabla}} \\ -\hat{\boldsymbol{\nabla}}^{\mathrm{T}} & \boldsymbol{0} \end{bmatrix} \right)^{-1} \boldsymbol{B}, \tag{3.24}$$

$$\boldsymbol{L}_s = \begin{bmatrix} -\mathrm{i}k_x U + \nu \, \hat{\nabla}^2 + D_s & -U' & 0 \\ 0 & -\mathrm{i}k_x U + \nu \, \hat{\nabla}^2 + D_s & 0 \\ 0 & 0 & -\mathrm{i}k_x U + \nu \, \hat{\nabla}^2 + D_s \end{bmatrix}, \tag{3.25}$$

$$D_s = -\sqrt{k_x^2 \, V_x^2(y) + k_z^2 \, V_z^2(y)} + \lambda_y(\boldsymbol{k}, y) \, \partial_y (V_y(y) \, \partial_y). \tag{3.26}$$
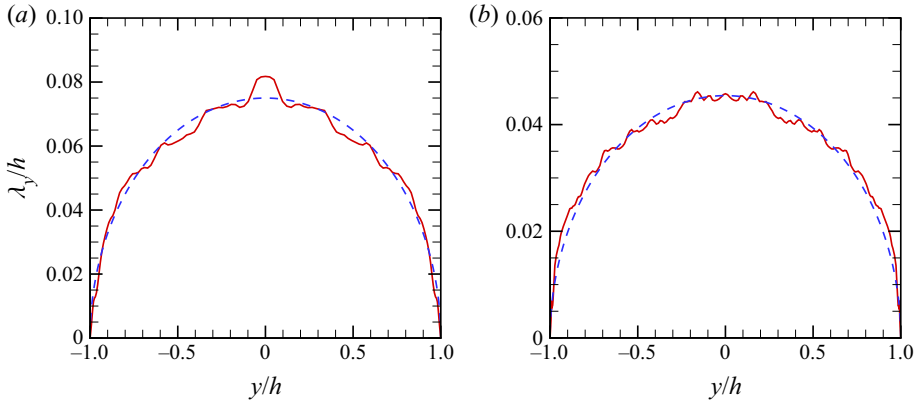
Figure 1. Characteristic length scale $\lambda_y(\mathbf{k}, y)$ of the turbulent channel flows at $\mathbf{k}h = (2, 4)$ for large-scale structures. (*a*) Plots for $Re_\tau = 180$, where the red solid line shows the DNS result, and the blue dashed line shows $0.075\sqrt{h^2 - y^2}$. (*b*) Plots for $Re_\tau = 550$, where the red solid line shows the DNS result, and the blue dashed line shows $0.046\sqrt{h^2 - y^2}$.

The operator $\mathbf{R}_s$ is called the sweeping-enhanced resolvent, analogous to the sweeping-enhanced transfer function R_s in the DAR model. In fact, it is the conventional resolvent operator augmented by the eddy damping term that appears on the diagonal of matrix $\mathbf{L}_s$. In § 3.3, we discuss the difference between the sweeping-enhanced resolvent and the eddy-viscosity-enhanced resolvent. Therefore, the space–time cross-spectrum of velocity fluctuations is given by

$$\boldsymbol{\Phi}_{\tilde{u}\tilde{u}} = \mathbf{R}_s \boldsymbol{\Phi}_{\tilde{f}\tilde{f}} \mathbf{R}_s^*, \tag{3.27}$$

where $\boldsymbol{\Phi}_{\tilde{u}\tilde{u}} = \langle \tilde{u}(\mathbf{k}, \omega, y)\, \tilde{u}^*(\mathbf{k}, \omega, y') \rangle$ is the space–time cross-spectrum of velocity fluctuations, and $\boldsymbol{\Phi}_{\tilde{f}\tilde{f}} = \langle \tilde{f}(\mathbf{k}, \omega, y)\tilde{f}^*(\mathbf{k}, \omega, y') \rangle$ is the space–time cross-spectrum of nonlinear forcing.

3.2. *Composition of the resolvents*

By analogy to (2.7) in the DAR model, the sweeping-enhanced resolvent $\mathbf{R}_s$ defined in (3.24) is applied to white-in-time random forcing $\tilde{f}_t$, yielding an intermediate random forcing $\tilde{f}$ of finite correlation time

$$\tilde{f} = \mathbf{R}_s \tilde{f}_t. \tag{3.28}$$

Subsequently, the obtained random forcing $\tilde{f}$ is used as the input to the same sweeping-enhanced resolvent as that in (3.28), leading to

$$\tilde{u} = \mathbf{R}_s \tilde{f}. \tag{3.29}$$

Therefore, the velocity fluctuation $\tilde{u}$ is determined by the random forcing $\tilde{f}_t$ through the composition of the sweeping-enhanced resolvent $\mathbf{R}_s$, that is,

$$\tilde{u} = \mathbf{R}_s^2 \tilde{f}_t. \tag{3.30}$$

It follows that the space–time cross-spectrum of velocity fluctuations is given by

$$\boldsymbol{\Phi}_{\tilde{u}\tilde{u}} = \mathbf{R}_s^2 \boldsymbol{\Phi}_{\tilde{f}_t \tilde{f}_t} \mathbf{R}_s^{*2}, \tag{3.31}$$

where $\boldsymbol{\Phi}_{\tilde{f}_t\tilde{f}_t} = \langle \tilde{\boldsymbol{f}}_t(\boldsymbol{k}, \omega, y)\tilde{\boldsymbol{f}}_t^*(\boldsymbol{k}, \omega, y')\rangle$ is the space–time cross-spectrum of the white-in-time random forcing $\tilde{\boldsymbol{f}}_t$. It is observed from (3.30) and (3.31) that the output and input are related by the composition of the sweeping-enhanced resolvent, $\boldsymbol{R}_s^2$. Accordingly, this composite resolvent is referred to as the $\boldsymbol{R}_s^2$ model.

The space–time cross-spectrum $\boldsymbol{\Phi}_{\tilde{f}_t\tilde{f}_t}$ of the random forcing $\tilde{\boldsymbol{f}}_t$ is calculated from

$$\boldsymbol{\Phi}_{\tilde{f}_t\tilde{f}_t}(\boldsymbol{k}, \omega, y, y') = \boldsymbol{I}[k_x^2\, V_x^2(y) + k_z^2\, V_z^2(y)]^{3/2}\langle v^2(y)\rangle\, \delta(y - y'). \qquad (3.32)$$

The space–time cross-spectrum depends on the variance of the wall-normal velocity fluctuations $\langle v^2(y)\rangle$ but is independent of the variances of streamwise and spanwise velocity fluctuations, $\langle u^2(y)\rangle$ and $\langle w^2(y)\rangle$. In fact, the wall-normal velocity fluctuations depend only on external forcing, as described by the Orr–Sommerfeld equation. However, the streamwise and spanwise velocity fluctuations depend on the wall-normal vorticity. According to the Squire equation, the wall-normal vorticity depends not only on external forcing but also on the energy production due to mean shear. The latter can be taken into account by the resolvent. Note that while the DAR model needs the spatial energy spectra of streamwise velocity fluctuations, the present $\boldsymbol{R}_s^2$ model needs only the variances of the velocity fluctuations. In the $\boldsymbol{R}_s^2$ model, the mean velocity $U(y)$, the r.m.s. of the velocity fluctuations $\sqrt{\langle u^2(y)\rangle}$, $\sqrt{\langle v^2(y)\rangle}$ and $\sqrt{\langle w^2(y)\rangle}$, and the factor $\beta(\boldsymbol{k})$ are taken from the DNS data.

Finally, we justify that the resolvent used in (3.28) is the same as that used in (3.29). In fact, the nonlinear forcing is found to exhibit space–time structures similar to those in turbulent flows (Morra *et al.* 2021; Nogueira *et al.* 2021), such as the streamwise vortices that are reminiscent of the streamwise vortex structures of velocity fluctuations. A different resolvent can be introduced to replace that used in (3.28). This offers more flexibility but definitely increases the number of undetermined parameters.

3.3. *Comparison of sweeping-enhanced and eddy-viscosity-enhanced resolvents*

The sweeping-enhanced resolvent is proposed in terms of the decorrelation process with the aim of predicting the space–time energy spectra. However, the eddy-viscosity-enhanced resolvent is based mainly on energy transfer. Although it is not yet used to predict space–time energy spectra, the eddy-viscosity-enhanced resolvent successfully reproduces the amplifications of coherent streaks and linear non-normal energy (Hwang & Cossu 2010*a*,*b*) and predicts the spatial energy spectra in the streamwise and spanwise directions (Gupta *et al.* 2021). In fact, Hwang & Cossu (2010*a*,*b*) introduced the eddy viscosity ν_t and random forcing $\boldsymbol{f}$ to represent the energy dissipation and extraction in the nonlinear forcing $\boldsymbol{F}$, leading to

$$\boldsymbol{F} = \nabla\cdot[\nu_t(\nabla\boldsymbol{u} + \nabla\boldsymbol{u}^{\mathrm{T}})] + \boldsymbol{f}. \qquad (3.33)$$

In turbulent channel flows, the Cess model is used widely for eddy viscosity. It should be noted that the eddy viscosity can also be calculated from the mean velocity and the Reynolds-averaged NS equations (Hwang & Cossu 2010*a*). The Cess model is written as

$$\nu_t(y) = \frac{\nu}{2}\sqrt{1 + \frac{\kappa^2\, Re_\tau^2}{9}\left(1 - \frac{y^2}{h^2}\right)^2\left(1 + \frac{2y^2}{h^2}\right)^2(1 - \exp(-y^+/A))^2} - \frac{\nu}{2}, \qquad (3.34)$$

where $\kappa = 0.426$ is the Kármán constant, A is a constant with $A = 25.4$, $y \in [-h, h]$ is the wall-normal location, and $y^+ = Re_\tau(1 - |y|/h)$. The eddy viscosity in the Cess model is independent of the length scales of turbulent eddies.

Gupta *et al.* (2021) proposed that the eddy viscosity should depend on the length scales of turbulent eddies as

$$\nu_t(\lambda, y) = \frac{\lambda}{\lambda + \lambda_m(y)} \, \nu_t(y), \tag{3.35}$$

$$\frac{\lambda_m(y)}{h} = \frac{50}{Re_\tau} + \left(2 - \frac{50}{Re_\tau}\right) \tanh\left[6\left(1 - \frac{|y|}{h}\right)\right], \tag{3.36}$$

where $\lambda = 2\pi/\sqrt{k_x^2 + k_z^2}$ is the wavelength. Here, $\nu_t(\lambda, y)$ becomes $\nu_t(y)$ for sufficiently large wavelengths $\lambda \to \infty$, and $\nu_t(\lambda, y)$ becomes zero for sufficiently small wavelengths $\lambda \to 0$.

Taking the spatial (x–z) Fourier transform of (3.33), we obtain the spatial Fourier mode $\hat{F}$ of the nonlinear forcing. Then substituting $\hat{F}$ into (3.3) and taking the temporal Fourier transform of (3.3) leads to the space–time Fourier mode $\tilde{u}$ of the velocity fluctuations:

$$\tilde{u} = R_{\nu_t}\tilde{f}, \tag{3.37}$$

where R_{ν_t} is referred to as the ν_t-enhanced resolvent that is given by

$$R_{\nu_t} = B^{\mathrm{T}}\left(-\mathrm{i}\omega\begin{bmatrix} I & \\ & 0 \end{bmatrix} - \begin{bmatrix} L_{\nu_{t_r}} & -\hat{\nabla} \\ -\hat{\nabla}^{\mathrm{T}} & 0 \end{bmatrix}\right)^{-1} B, \tag{3.38}$$

$$L_{\nu_t} = \begin{bmatrix} -\mathrm{i}k_x U + \nu_T \hat{\nabla}^2 + \nu_T' \partial_y & -U' + \mathrm{i}k_x \nu_T' & 0 \\ 0 & -\mathrm{i}k_x U + \nu_T \hat{\nabla}^2 + 2\nu_T' \partial_y & 0 \\ 0 & \mathrm{i}k_z \nu_T' & -\mathrm{i}k_x U + \nu_T \hat{\nabla}^2 + \nu_T' \partial_y \end{bmatrix}, \tag{3.39}$$

with $\nu_T = \nu + \nu_t$. Note that the ν_t-enhanced resolvent R_{ν_t} in (3.38) with $\nu_t = 0$ becomes the resolvent R in (3.7). Therefore, the space–time cross-spectrum of the velocity is

$$\Phi_{\tilde{u}\tilde{u}} = R_{\nu_t}\Phi_{\tilde{f}\tilde{f}}R_{\nu_t}^*. \tag{3.40}$$

In LNSEs and resolvent-based methods, white forcing is used widely (Farrell & Ioannou 1998; Bamieh & Dahleh 2001; Jovanović & Bamieh 2005; Liu & Gayme 2020; Gupta *et al.* 2021). The forcing intensity is usually taken as constant in the wall-normal direction (Morra *et al.* 2019):

$$\Phi_{\tilde{f}\tilde{f}}(k, \omega, y, y') = I\,\delta(y - y'), \tag{3.41}$$

which is used in the B model (see § 4).

Gupta *et al.* (2021) further proposed that the forcing intensity depends on the eddy viscosity as

$$\Phi_{\tilde{f}\tilde{f}}(k, \omega, y, y') = I\,\nu_t^2(y)\,\delta(y - y'), \tag{3.42}$$

where the Cess model is used for ν_t. The forcing spectra in (3.42) are used in the W model (see § 4). Similarly, the Cess model can be replaced by the wavelength-dependent eddy viscosity (3.35) and (3.36), giving

$$\Phi_{\tilde{f}\tilde{f}}(k, \omega, y, y') = I\,\nu_t^2(\lambda, y)\,\delta(y - y'). \tag{3.43}$$

The forcing spectra in (3.43) are used in the λ model (see § 4).

956 A31-12

Therefore, both eddy viscosity and random forcing depend not only on the wall-normal locations but also on the wavenumbers. Consequently, the λ model proposed by Gupta *et al.* (2021) with $\nu_t(\lambda, y)$ and the wall-distance dependence of the forcing intensity accounts for the energy transfer along the wall-normal direction, and the energy transfer between different length scales in space. Therefore, this model correctly predicts the two-dimensional spatial spectra. However, this cannot ensure the correct prediction of frequency spectra and time correlations.

The eddy viscosity and sweeping velocity lead to different characteristic decay times, as shown in figures 7 and 8, while both give rise to temporal decorrelation of coherent structures. In fact, as the wall distance increases, the eddy viscosity in the logarithmic region becomes larger and thus gives rise to smaller characteristic decay time scales. This is in contrast to the decorrelation process in turbulent channel flows, where the characteristic decay time scales become larger with increasing wall distance. It is noted in (3.34) that the eddy viscosity in the logarithmic region is $\nu_t(y) = u_\tau \kappa d$, where the wall distance is given by $d = 1 - |y|/h$, and κd is the mixing length. However, as the wall distance increases, the sweeping velocities decrease and thus give rise to larger characteristic decay time scales. This is consistent with the observation that the time correlations in turbulent channel flows decay more slowly with increasing wall distance.

Van Atta & Wyngaard (1975) pointed out that the high-order spectra are related to the energy spectra of velocity fluctuations through the random sweeping velocity. This result was justified theoretically and validated by Praskovsky *et al.* (1993), Katul *et al.* (2016) and Huang & Katul (2022). Note that the spectra of nonlinear forcing are the fourth-order moments of velocity fluctuations, and the energy spectra are the second-order moments of velocity fluctuations. Therefore, the spectra of nonlinear forcing are related to the velocity spectra through the random sweeping velocity, supporting the sweeping-enhanced resolvent in the present study.

4. Numerical results

Two sets of DNS of turbulent channel flows at $Re_\tau = 180$ and 550 are performed in this work. The NS equations are solved using a pseudo-spectral method with a 3/2 de-aliasing rule. Periodic boundary conditions are applied in the streamwise and spanwise directions, and no-slip conditions are applied at the walls. For the case $Re_\tau = 180$, the computational domain is $8\pi h \times 2h \times 4\pi h$ in the streamwise (x), wall-normal (y) and spanwise (z) directions. The $384 \times 128 \times 384$ grid is used. The time step is $5 \times 10^{-3} h/U_b$, where U_b is the bulk velocity. In the statistically stationary state, the instantaneous flow fields are stored every 10 steps, and a total of 5000 steps are stored. For the case $Re_\tau = 550$, the computational domain is $4\pi h \times 2h \times 2\pi h$ in the streamwise, wall-normal and spanwise directions, respectively. The $576 \times 256 \times 576$ grid is used. The time step is $1 \times 10^{-3} h/U_b$. In the statistically stationary state, the instantaneous flow fields are stored every 50 steps, and a total of 5400 steps are stored. The NS solver and dataset have been validated in previous studies (Wu *et al.* 2017; Wu & He 2020, 2021*b*).

To perform the temporal Fourier transform, the Hanning window is used with a 50 % overlap and window length $51.2h/U_b$. The spanwise length scale of large-scale structures in wall turbulence is $\lambda_z \approx h$–$1.5h$, and the streamwise length scale is $\lambda_x \approx 2\lambda_z$ (Kim & Adrian 1999; Smits, McKeon & Marusic 2011; Morra *et al.* 2019). Therefore, the wavenumber range of large-scale structures is $k_z h = 2\pi h/\lambda_z \approx 4$–6 and $k_x \approx k_z/2$. In this paper, the wavenumber vector $(k_x h, k_z h) = (2, 4)$ is taken for the analysis of the large-scale structures.

Model	Resolvent	Forcing spectra
ν model	$\boldsymbol{R}$	$\boldsymbol{I}\delta(y - y')$
	see (3.7)	see (3.41)
B model	$\boldsymbol{R}_{\nu_t}$ with $\nu_t(y)$	$\boldsymbol{I}\,\delta(y - y')$
	see (3.34) and (3.38)	see (3.41)
W model	$\boldsymbol{R}_{\nu_t}$ with $\nu_t(y)$	$\boldsymbol{I}\,\nu_t^2(y)\,\delta(y - y')$
	see (3.34) and (3.38)	see (3.42)
λ model	$\boldsymbol{R}_{\nu_t}$ with $\nu_t(\lambda, y)$	$\boldsymbol{I}\,\nu_t^2(\lambda, y)\,\delta(y - y')$
	see (3.38) and (3.35)	see (3.43)
$\boldsymbol{R}_s^2$ model	$\boldsymbol{R}_s^2$ with D_s	$\boldsymbol{I}\,[k_x^2\,V_x^2(y) + k_z^2\,V_z^2(y)]^{3/2}\langle v^2(y)\rangle\,\delta(y - y')$
	see (3.24), (3.26) and (3.31)	see (3.32)

Table 1. Summary of the resolvent-based models used in the present study.

Five resolvent-based models are used in this work, and the settings (i.e. resolvent and forcing spectra) of these models are shown in table 1. The model with neither eddy viscosity nor sweeping is referred to as the ν model (Morra *et al.* 2019), and the three models with eddy viscosity are referred to as the B model, W model and λ model (Gupta *et al.* 2021). We use the following symbols for the eddy-viscosity-enhanced models in Gupta *et al.* (2021): 'B' in the B model refers to baseline, where the forcing spectrum is uniform in the wall-normal direction; 'W' in the W model refers to wall-distance dependence, where the forcing spectrum depends on the wall distance; and 'λ' in the λ model indicates that the eddy viscosity and forcing spectrum depend on the wavelength λ. The $\boldsymbol{R}_s^2$ model refers to the proposed model in this paper. In the following, we use these models to predict the space–time statistics of the large-scale structures in turbulent channel flows, and compare these predictions with the DNS results.

The space–time energy spectrum, or one-point wavenumber–frequency spectrum, of the streamwise velocity fluctuation is expressed as

$$\Phi(\boldsymbol{k}, \omega, y) = \langle \tilde{u}(\boldsymbol{k}, \omega, y)\,\tilde{u}^*(\boldsymbol{k}, \omega, y)\rangle, \tag{4.1}$$

where $\tilde{u}(\boldsymbol{k}, \omega, y)$ is the space–time Fourier mode of the streamwise velocity fluctuation. The space–time cross-spectrum, or two-point wavenumber–frequency cross-spectrum, of the streamwise velocity fluctuation is expressed as

$$\Phi(\boldsymbol{k}, \omega, y, y') = \langle \tilde{u}(\boldsymbol{k}, \omega, y)\,\tilde{u}^*(\boldsymbol{k}, \omega, y')\rangle. \tag{4.2}$$

In the numerical calculation, $\tilde{\boldsymbol{u}}$ is a column vector of size $3N$, given by

$$\tilde{\boldsymbol{u}} = \big[\tilde{u}(y_1), \ldots, \tilde{u}(y_i), \ldots, \tilde{u}(y_N), \tilde{v}(y_1), \ldots, \tilde{v}(y_i), \ldots, \tilde{v}(y_N),$$
$$\tilde{w}(y_1), \ldots, \tilde{w}(y_i), \ldots, \tilde{w}(y_N)\big]^{\mathrm{T}}, \tag{4.3}$$

where y_i is the wall-normal coordinate of the ith grid point ($i = 1, \ldots, N$), N is the number of wall-normal grid points, and 3 denotes the number of velocity components; $\boldsymbol{\Phi}_{\tilde{u}\tilde{u}}$ in (3.31) and (3.40) is a matrix of size $3N \times 3N$. In the matrix $\boldsymbol{\Phi}_{\tilde{u}\tilde{u}}$, the (i, j)th element represents the space–time cross-spectrum $\Phi(\boldsymbol{k}, \omega, y_i, y_j)$, and the (i, i)th element represents the space–time energy spectrum $\Phi(\boldsymbol{k}, \omega, y_i)$.

We focus on the streamwise velocity spectral distribution in the frequency (ω) and wall-normal (y) directions. Integrating the space–time energy spectrum over ω and y, we
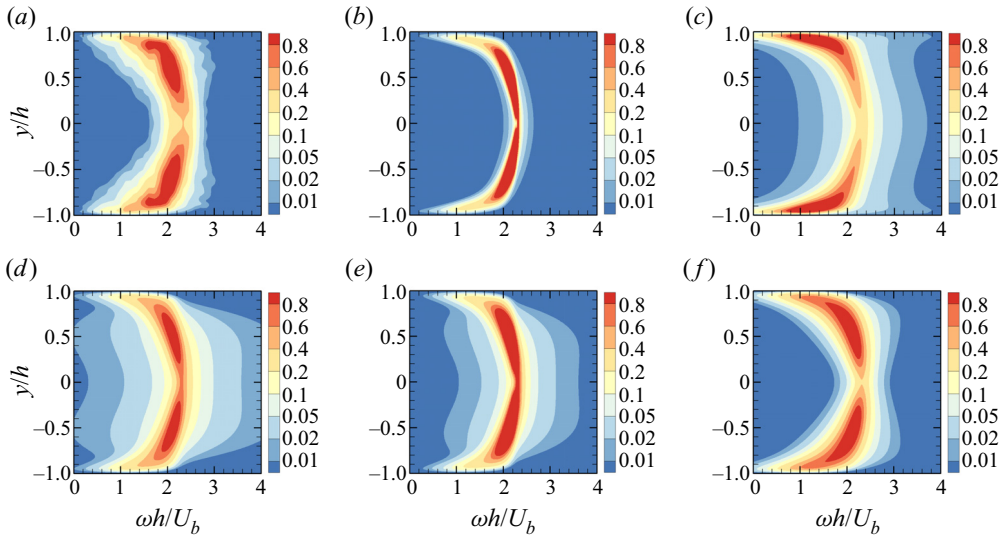
Figure 2. Frequency spectral distributions in the wall-normal direction, $\Phi(\boldsymbol{k}, \omega, y)/\Phi_I(\boldsymbol{k})$, at $\boldsymbol{k}h = (2, 4)$ for large-scale structures at $Re_\tau = 180$: (*a*) DNS, (*b*) ν model, (*c*) B model, (*d*) W model, (*e*) λ model, (*f*) $\boldsymbol{R}_s^2$ model.

obtain the total streamwise velocity energy

$$\Phi_I(\boldsymbol{k}) = \int_{-h}^{h} \mathrm{d}y \int_{-\infty}^{\infty} \mathrm{d}\omega \, \Phi(\boldsymbol{k}, \omega, y), \tag{4.4}$$

which is used as the normalization factor to obtain the streamwise velocity spectral distribution. We note that the spectral distributions from the DNS and those models are normalized by their corresponding integrated spectrum in (4.4).

Figures 2 and 3 plot the frequency spectral distributions in the wall-normal direction, $\Phi(\boldsymbol{k}, \omega, y)/\Phi_I(\boldsymbol{k})$, at $\boldsymbol{k}h = (2, 4)$ for large-scale structures at the two Reynolds numbers $Re_\tau = 180$ and 550, respectively. The $\boldsymbol{R}_s^2$ model reproduces the curved ribbon region in the DNS, in which the coloured contours of the same levels have similar locations, areas and shapes. The red-ribbon region of the largest level in the ν model is relatively narrow, as was also observed by Morra *et al.* (2019). The regions of coloured ribbons in the B model, the W model and the λ model are spread over broader ranges of frequencies compared to the DNS results because the eddy viscosity gives rise to smaller decorrelation time scales and thus larger energy-contained frequencies. In particular, the red ribbons in the B model are concentrated in the near-wall region because the eddy viscosities used in this model are incorrectly larger in the outer-layer region and smaller in the near-wall region. The forcing intensity used in the W model depends on the wall-normal locations, balancing the effect of the eddy viscosity dependent on the wall-normal locations, and leading to red and yellow regions that are similar to those for the DNS results. However, the eddy viscosity in the λ model is smaller than that in the W model and thus reduces the extent of the ribbon-like frequency regions. We note that both the sweeping term and the forcing intensity in the $\boldsymbol{R}_s^2$ model depend on the wall-normal locations and characteristic length scales of the turbulent eddies, and that the frequency spectral distribution in the wall-normal direction is consistent with that for the DNS results.

The differences between the space–time energy spectra obtained by the above models and by the DNS can be quantified using the Hellinger distance (Wu & He 2020, 2021*b*)
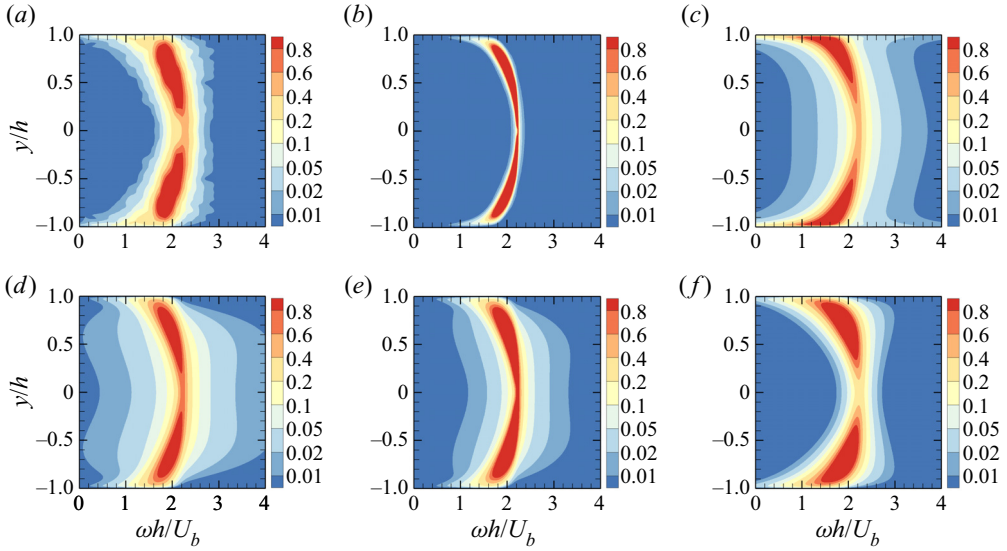
Figure 3. Frequency spectral distributions in the wall-normal direction, $\Phi(\boldsymbol{k}, \omega, y)/\Phi_I(\boldsymbol{k})$, at $\boldsymbol{k}h = (2, 4)$ for large-scale structures at $Re_\tau = 550$: (*a*) DNS, (*b*) ν model, (*c*) B model, (*d*) W model, (*e*) λ model, (*f*) $\boldsymbol{R}_s^2$ model.
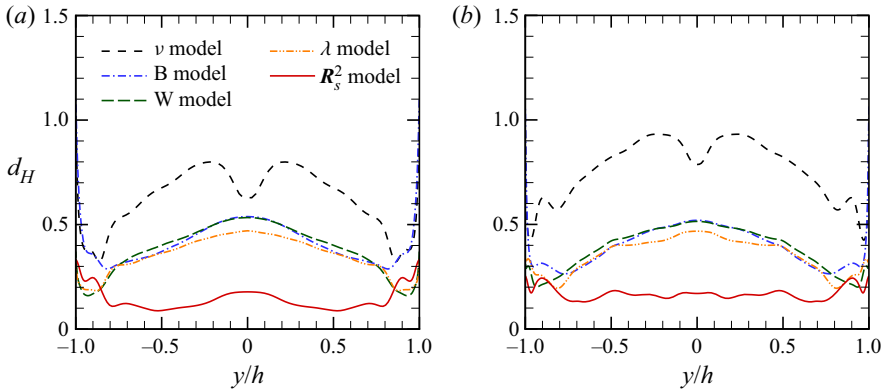
Figure 4. Hellinger distance $d_H(\boldsymbol{k}, y)$ at $\boldsymbol{k}h = (2, 4)$ for large-scale structures: (*a*) $Re_\tau = 180$, (*b*) $Re_\tau = 550$.

that is defined as

$$
d_H(\boldsymbol{k}, y) = \left[\int \left(\sqrt{\frac{\Phi^{model}(\boldsymbol{k}, \omega, y)}{\Phi^{model}(\boldsymbol{k}, y)}} - \sqrt{\frac{\Phi^{DNS}(\boldsymbol{k}, \omega, y)}{\Phi^{DNS}(\boldsymbol{k}, y)}} \right)^2 \mathrm{d}\omega \right]^{1/2}. \quad (4.5)
$$

Figure 4 shows the Hellinger distance $d_H(\boldsymbol{k}, y)$ at $\boldsymbol{k}h = (2, 4)$ for large-scale structures. The Hellinger distances between the ν model and the DNS results are the largest. In the near-wall region, the Hellinger distances from the W model, λ model and $\boldsymbol{R}_s^2$ model are similar. However, in most regions of the channel, the Hellinger distances from the $\boldsymbol{R}_s^2$ model are significantly smaller than those from other models, implying that the $\boldsymbol{R}_s^2$ model is more consistent with the DNS results.

956 A31-16
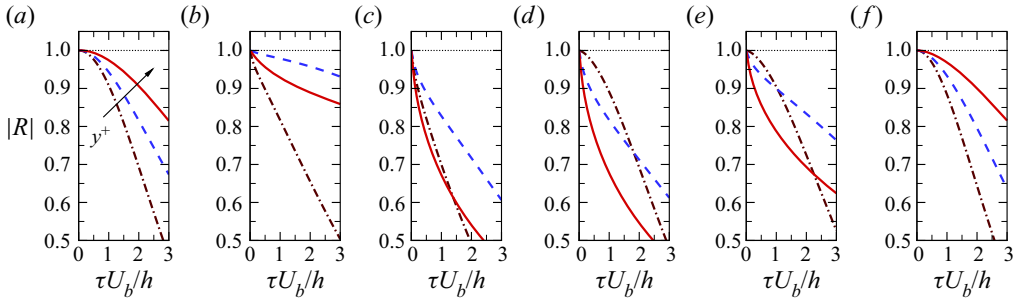
Figure 5. Amplitude of the time correlations $|R(\boldsymbol{k}, \tau, y)|$ at $\boldsymbol{k}h = (2, 4)$ for large-scale structures and at three wall-normal locations at $Re_\tau = 180$. Red solid lines, $y^+ = 180$; blue dashed lines, $y^+ = 50$; brown dash-dotted lines, $y^+ = 5$. (a) DNS, (b) ν model, (c) B model, (d) W model, (e) λ model, (f) $\boldsymbol{R}_s^2$ model.

The resolvent models are examined in terms of the time correlations of the spatial Fourier modes at a fixed wavenumber and one wall-normal location that are given by

$$R(\boldsymbol{k}, \tau, y) = \frac{\displaystyle\int_{-\infty}^{\infty} \Phi(\boldsymbol{k}, \omega, y) \exp(-i\omega\tau) \, d\omega}{\displaystyle\int_{-\infty}^{\infty} \Phi(\boldsymbol{k}, \omega, y) \, d\omega}. \tag{4.6}$$

Figures 5 and 6 show the time correlations $|R(\boldsymbol{k}, \tau, y)|$ at $\boldsymbol{k}h = (2, 4)$ for large-scale structures and at three wall-normal locations: $y^+ = 5$, 50 and 180 for $Re_\tau = 180$, and $y^+ = 5$, 92 and 550 for $Re_\tau = 550$. The time correlations in the two cases exhibit consistent decay behaviours. Accordingly, we discuss only the case for $Re_\tau = 550$. It is observed from the DNS that the time correlation at $y^+ = 92$ decays more rapidly than that at $y^+ = 550$, while the time correlation at $y^+ = 5$ shows the fastest decays. The R_s^2 model reproduces the DNS results, where the decay becomes slower with increasing wall-normal distance. However, the resolvent model without eddy viscosity (ν model) and the eddy-viscosity-enhanced models (B model, W model and λ model) give decay behaviours that are inconsistent with the DNS results, where the time correlations at $y^+ = 92$ decay more slowly than those at $y^+ = 550$. Furthermore, due to the composition of the sweeping-enhanced resolvent, the time correlations in figure 6(f) gradually decrease over a short time, which is in agreement with the DNS results. However, the time correlations obtained from the ν model, B model, W model and λ model fall steeply at short times since the white-in-time external forcing acts on the velocity modes and thus leads to vanishing Taylor time microscales.

To quantify the short-time decay of the time correlations predicted by the resolvent models, we introduce the characteristic decay time scales as follows:

$$|R(\boldsymbol{k}, \tau = T_d, y)| = R_d. \tag{4.7}$$

The characteristic decay time scale $T_d(\boldsymbol{k}, y)$ is that for which the time correlations decay to a certain value R_d, and describes the effects of white-in-time external forcing on time correlations. In this paper, we take $R_d = 0.9$. Different values of R_d (e.g. $R_d = 0.95$ and 0.8) are also taken, and the obtained results (not shown in this paper) do not change the conclusions.

Figures 7 and 8 compare the characteristic decay time scales obtained from the resolvent-based models and the DNS at $\boldsymbol{k}h = (2, 4)$ for $Re_\tau = 180$ and 550, respectively.
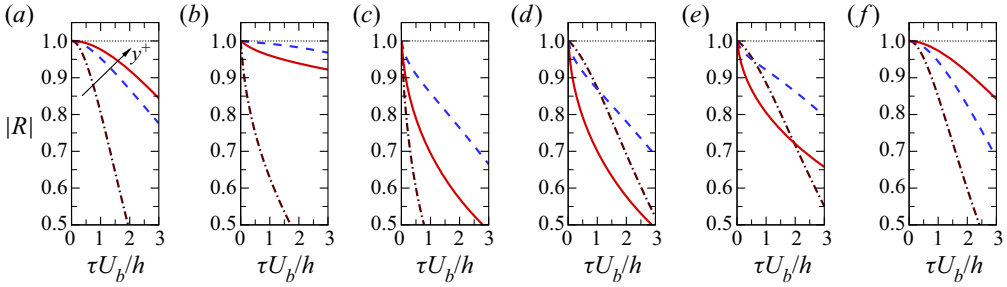
Figure 6. Amplitude of the time correlations $|R(\mathbf{k}, \tau, y)|$ at $\mathbf{k}h = (2, 4)$ for large-scale structures and at three wall-normal locations at $Re_\tau = 550$. Red solid lines, $y^+ = 550$; blue dashed lines, $y^+ = 92$; brown dash-dotted lines, $y^+ = 5$. (*a*) DNS, (*b*) ν model, (*c*) B model, (*d*) W model, (*e*) λ model, (*f*) $\mathbf{R}_s^2$ model.

To illustrate the necessity of composite resolvents, we compare the compositions of the resolvents, such as the ν^2 model, B^2 model, W^2 model, λ^2 model and $\mathbf{R}_s^2$ model, with the resolvents themselves, the ν model, B model, W model, λ model and $\mathbf{R}_s$ model. The characteristic time scales in the DNS increase with increasing wall distance. However, the characteristic time scales for the ν model are significantly larger than those for the DNS results. The eddy-viscosity-enhanced resolvent models, such as the B model, the W model and the λ model, significantly underpredict the DNS results. Furthermore, the obtained time scales increase in the near-wall region and incorrectly decrease in other regions. In the outer region, the characteristic time scales of the $\mathbf{R}_s$ model increase with increasing wall distance, which is consistent with the DNS results. However, they are one order of magnitude smaller than the DNS results. The characteristic time scales of the composite resolvents are significantly larger than those of the single resolvents. Consequently, the ν^2 model yields larger characteristic time scales than those obtained using the ν model. The characteristic time scales of the B^2 model, W^2 model and λ^2 model increase with increasing wall distance, which is consistent with the DNS results. Therefore, compared with eddy-viscosity-enhanced resolvents, their composite models improve the characteristic time scales. However, the characteristic time scales obtained from these models are larger than those obtained from the DNS. Since the eddy viscosity of the λ^2 model is smaller than that of the W^2 model, the characteristic time scales from the λ^2 model are between the results of the W^2 model and the results of the ν^2 model. The characteristic time scales obtained from the $\mathbf{R}_s^2$ model are in good agreement with the DNS results. In fact, the $\mathbf{R}_s^2$ model includes the three essential elements: LNSE, random sweeping and random forcing. Therefore, it can reproduce the time correlations in the central region where random sweeping is dominant, and the time correlations in the near-wall region where in addition to random sweeping the mean shear, molecular viscosity and pressure play important roles.

In addition to the wavenumber vector $\mathbf{k}h = (2, 4)$, we calculate the frequency spectral distributions and characteristic time scales at $\mathbf{k}h = (1, 2)$ and $\mathbf{k}h = (4, 8)$ for large-scale structures. The results (see Appendix A) show that the frequency spectral distributions and wall-normal variation trends of the characteristic time scales obtained using the $\mathbf{R}_s^2$ model are consistent with the DNS results. We further calculate the characteristic time scales obtained from the resolvent-based models at $\mathbf{k}h = (2, 4)$ for $Re_\tau = 1000$ (see Appendix B). The results are similar to those at $Re_\tau = 180$ and 550, implying the
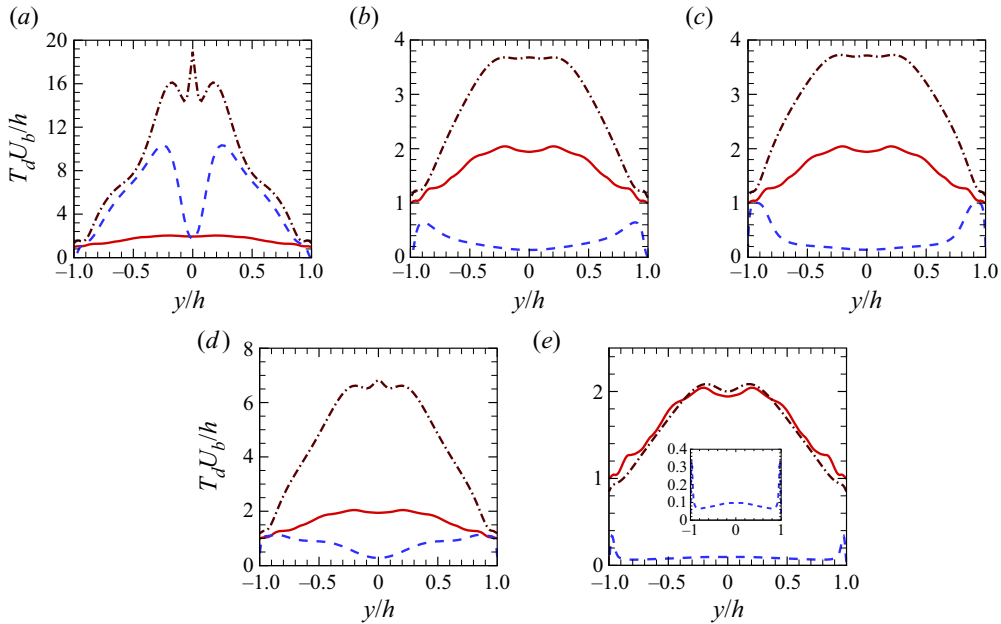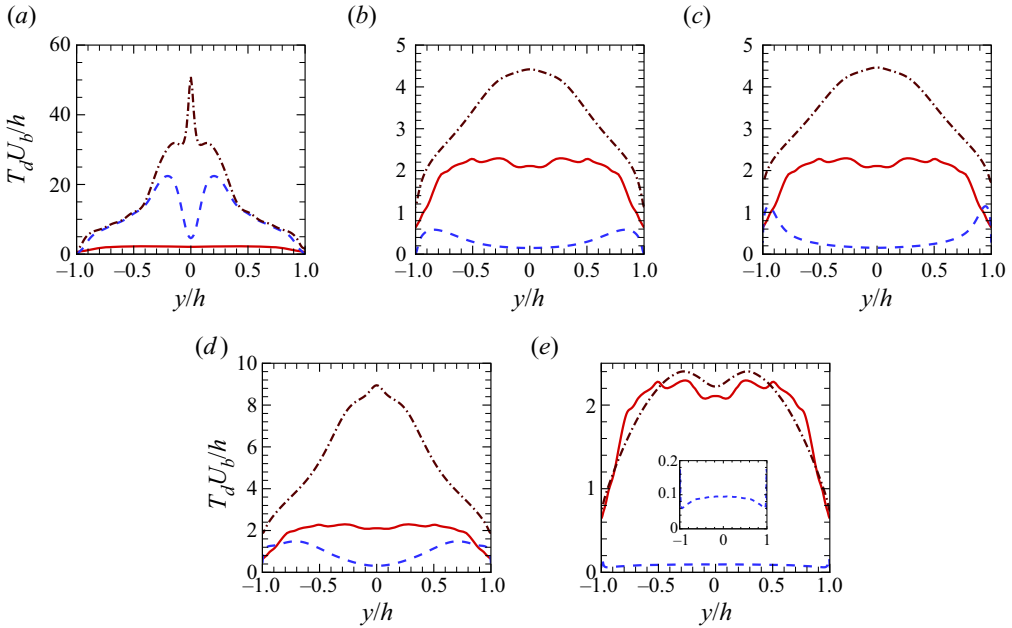
956 A31-18

Figure 7. Comparison of the characteristic decay time scales obtained by the resolvent-based models with the DNS at $kh = (2, 4)$ for $Re_\tau = 180$. Red solid lines, the DNS results; blue dashed lines, the results of the (*a*) ν model, (*b*) B model, (*c*) W model, (*d*) λ model, and (*e*) $\boldsymbol{R}_s$ model; brown dash-dotted lines, the results of the (*a*) ν^2 model, (*b*) B^2 model, (*c*) W^2 model, (*d*) λ^2 model, and (*e*) $\boldsymbol{R}_s^2$ model. The inset in (*e*) shows an enlarged view of the result of the $\boldsymbol{R}_s$ model.

applicability of the $\boldsymbol{R}_s^2$ model at higher Reynolds numbers. Although this paper focuses on the streamwise velocity fluctuations, we also calculate the frequency spectral distributions and characteristic time scales of the spanwise and wall-normal velocity fluctuations of the wavenumber vectors $kh = (1, 2)$, $kh = (2, 4)$ and $kh = (4, 8)$ (see Appendix C), and the results obtained from the $\boldsymbol{R}_s^2$ model are also consistent with the DNS results.

Figure 9 compares the Taylor time microscales obtained using the $\boldsymbol{R}_s^2$ model with the DNS results at $kh = (2, 4)$. According to Wu & He (2021*b*), the Taylor time microscales obtained by the direct imposition of white-in-time random forcing are zero. Due to the composition of resolvents, the $\boldsymbol{R}_s^2$ model can yield non-zero Taylor time microscales $\lambda_T(\boldsymbol{k}, y)$ of the time correlation $|R(\boldsymbol{k}, \tau, y)|$, where Taylor time microscale $\lambda_T(\boldsymbol{k}, y)$ is defined as

$$\lambda_T(\boldsymbol{k}, y) = [- (1/2)\partial_{\tau\tau}^2 |R(\boldsymbol{k}, \tau, y)|\big|_{\tau=0}]^{-1/2}. \tag{4.8}$$

The Taylor time microscales obtained by the $\boldsymbol{R}_s^2$ model are in good agreement with the DNS results, particularly at $Re_\tau = 550$.

Figure 10 compares the integral time scales T_I at $kh = (2, 4)$ for the $\boldsymbol{R}_s^2$ model with the DNS results. The integral time scale T_I of the time correlation is defined as

$$T_I = \int_0^{\tau_0} |R(\boldsymbol{k}, \tau, y)| \, d\tau, \tag{4.9}$$

where τ_0 is determined by $|R(\boldsymbol{k}, \tau_0, y)| = 0.2$. Due to the limited number of samples, the time correlations $|R(\boldsymbol{k}, \tau, y)|$ of the DNS oscillate at large separations. Therefore, the upper

956 A31-19

Figure 8. Comparison of the characteristic decay time scales obtained by the resolvent-based models with the DNS at $kh = (2, 4)$ for $Re_\tau = 550$. Red solid lines, the DNS results; blue dashed lines, the results of the (*a*) v model, (*b*) B model, (*c*) W model, (*d*) λ model, and (*e*) R_s model; brown dash-dotted lines, the results of the (*a*) v^2 model, (*b*) B^2 model, (*c*) W^2 model, (*d*) λ^2 model, and (*e*) R_s^2 model. The inset in (*e*) shows an enlarged view of the result of the R_s model.
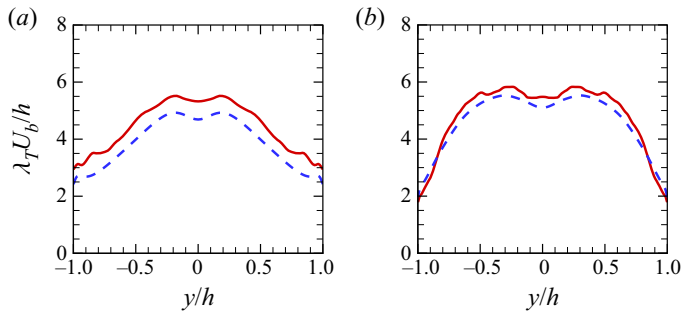
Figure 9. Comparison of the Taylor time microscales $\lambda_T(k, y)$ from the R_s^2 model with the DNS results at $kh = (2, 4)$. Red solid lines, the DNS results; blue dashed lines, the results of the R_s^2 model. Plots for (*a*) $Re_\tau = 180$, (*b*) $Re_\tau = 550$.

limit of the integration in (4.9) is taken as τ_0 for $|R(k, \tau_0, y)| = 0.2$. The results of the R_s^2 model are close to those obtained by the DNS, with only slight differences.
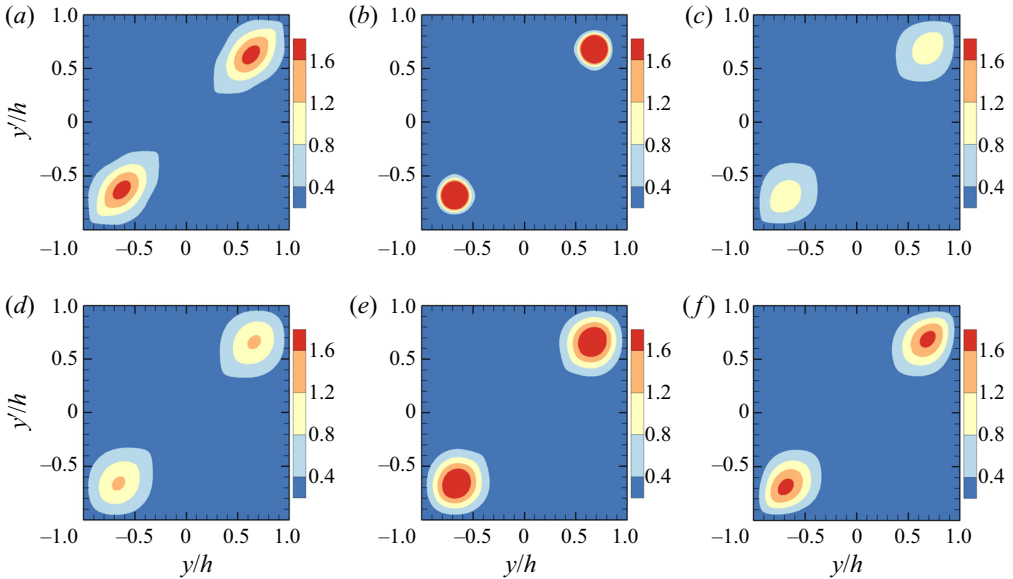
Figures 11 and 12 show the cross-spectral distribution $|\Phi(k, \omega_p, y, y')|/\Phi_I(k)$ of the streamwise velocity modes at $kh = (2, 4)$ for large-scale structures, and the peak frequencies $\omega_p h/U_b = 2.1$ for $Re_\tau = 180$, and $\omega_p h/U_b = 2$ for $Re_\tau = 550$. It is noted that the cross-spectral distribution at the given wavenumber vector and frequency is the correlation of the space–time Fourier modes at two wall-normal positions. The peak frequency is determined by maximizing the total frequency spectral distribution at the

956 A31-20
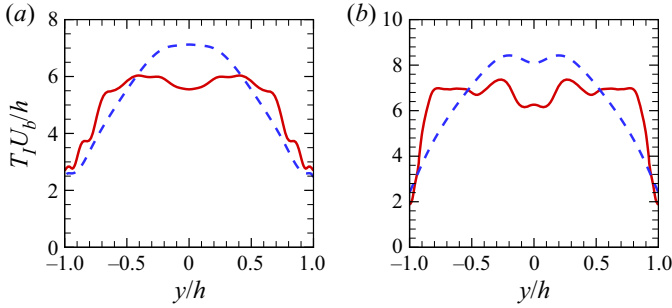
Figure 10. Comparison of the integral time scales T_I from the R_s^2 model with the DNS results at $kh = (2, 4)$. Red solid lines, the DNS results; blue dashed lines, the results of the R_s^2 model. Plots for (*a*) $Re_\tau = 180$, (*b*) $Re_\tau = 550$.
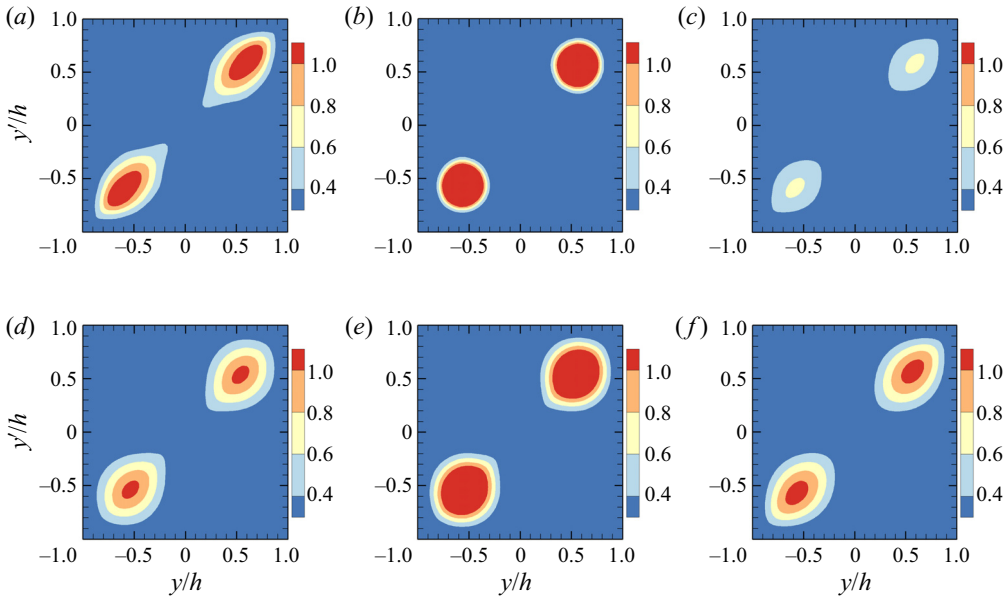
Figure 11. Amplitude of the cross-spectral distribution $|\Phi(k, \omega_p, y, y')|/\Phi_I(k)$ of the streamwise velocity modes at $kh = (2, 4)$ for large-scale structures and the peak frequency $\omega_p h/U_b = 2.1$ for $Re_\tau = 180$: (*a*) DNS, (*b*) ν model, (*c*) B model, (*d*) W model, (*e*) λ model, (*f*) R_s^2 model.

given wavenumber:

$$\Phi_T(k, \omega) = \frac{\displaystyle\int_{-h}^{h} \Phi(k, \omega, y) \, \mathrm{d}y}{\Phi_I(k)}. \tag{4.10}$$

The cross-spectral distributions in the two Reynolds numbers exhibit similar behaviours. Accordingly, we discuss only the case for $Re_\tau = 550$. It is observed from the DNS that the cross-spectral distribution is maximal along the diagonal line $y = y'$ and decays most rapidly in the direction normal to the diagonal line. The R_s^2 model reproduces the results observed for the DNS. In particular, it reproduces the coloured contours of different levels, namely their elliptical shapes and areas. The eddy-viscosity-enhanced model improves the predictions of the shapes and areas of coloured contours (see figures 12*c*,*d*)), and the

956 A31-21

Figure 12. Amplitude of the cross-spectral distribution $|\Phi(\boldsymbol{k}, \omega_p, y, y')|/\Phi_I(\boldsymbol{k})$ of the streamwise velocity modes at $\boldsymbol{k}h = (2, 4)$ for large-scale structures and the peak frequency $\omega_p h/U_b = 2$ for $Re_\tau = 550$: (a) DNS, (b) ν model, (c) B model, (d) W model, (e) λ model, (f) $\boldsymbol{R}_s^2$ model.
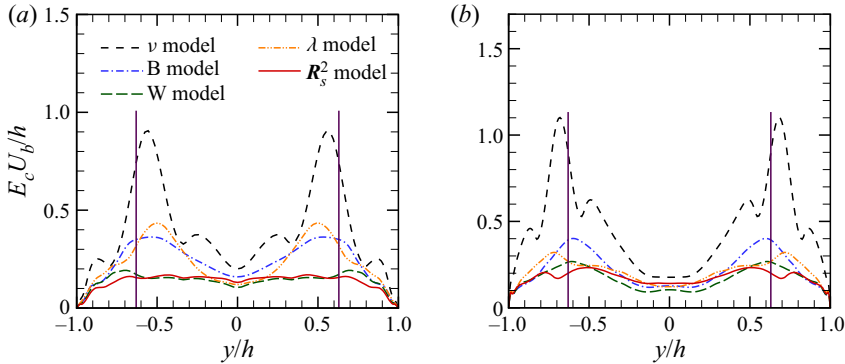
Figure 13. Errors $E_c(\boldsymbol{k}, \omega_p, y)$ in the cross-spectral distributions obtained by different models relative to the DNS results at $\boldsymbol{k}h = (2, 4)$: (a) $Re_\tau = 180$, (b) $Re_\tau = 550$. Two vertical lines are shown at $|y/h| = 0.63$ to indicate the peaks of the cross-spectral distributions.

gradual changes of the coloured contours (see figure 12*e*). However, the spectral peaks are underpredicted in figure 12(*c*) and overpredicted in figure 12(*e*). Note that the DAR model cannot predict the wall-normal two-point cross-spectra. However, the prediction of the cross-spectra can be achieved by the $\boldsymbol{R}_s^2$ model, where an LNSE is used to replace Taylor's frozen-flow model in the DAR model.

The differences in the cross-spectral distribution between the models and the DNS can be quantified using the function $E_c(\boldsymbol{k}, \omega_p, y)$, defined as

$$E_c(\boldsymbol{k}, \omega_p, y) = \int \left| \frac{|\Phi^{model}(\boldsymbol{k}, \omega_p, y, y')|}{\Phi_I^{model}(\boldsymbol{k})} - \frac{|\Phi^{DNS}(\boldsymbol{k}, \omega_p, y, y')|}{\Phi_I^{DNS}(\boldsymbol{k})} \right| \mathrm{d}y'. \qquad (4.11)$$
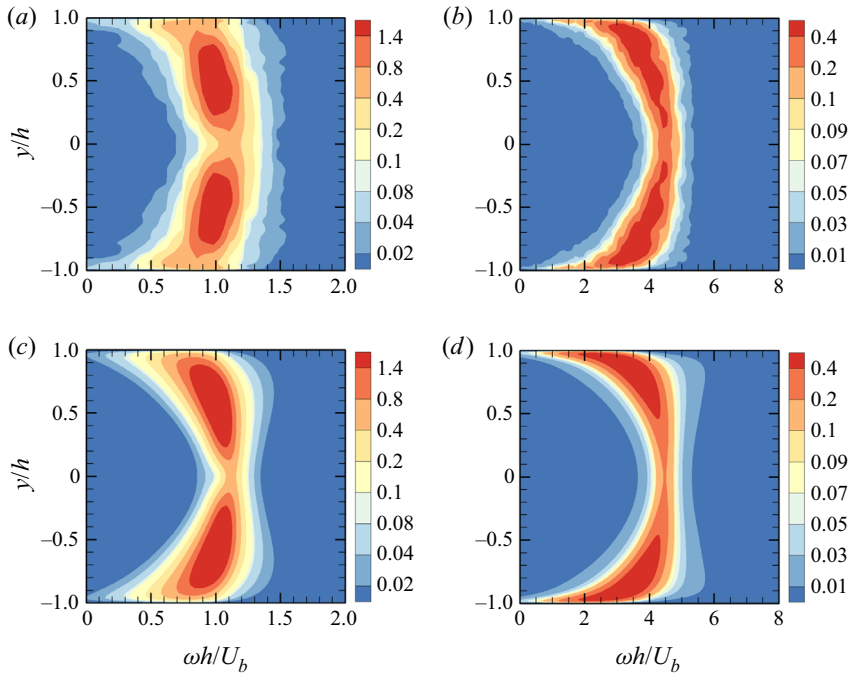
956 A31-22
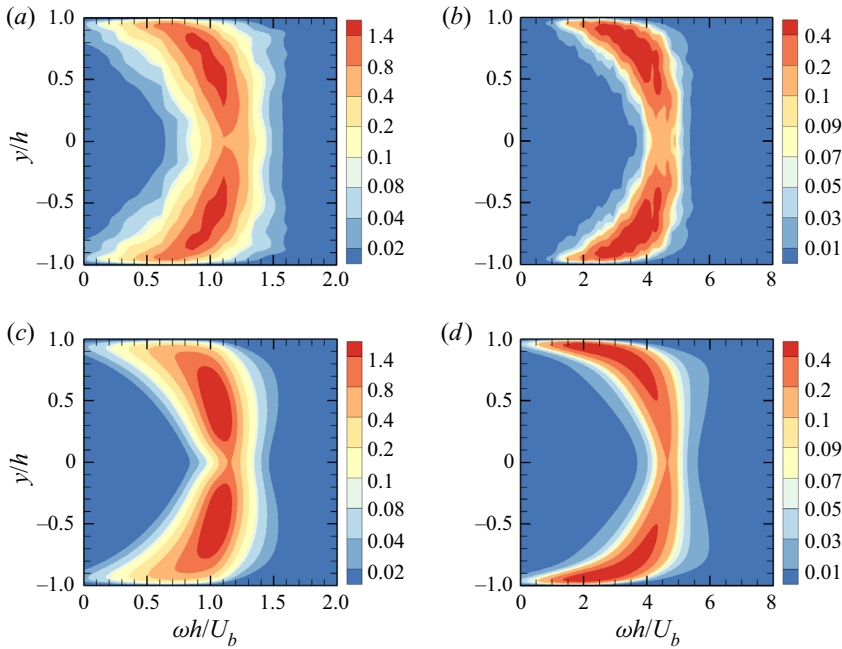
Figure 14. Frequency spectral distributions at (a,c) $kh = (1, 2)$ and (b,d) $kh = (4, 8)$ in the turbulent channel flows at $Re_\tau = 180$: (a,b) DNS results; (c,d) Results of the R_s^2 model.

The function $E_c(k, \omega_p, y)$ measures the error in the cross-spectral distribution of the model relative to the DNS result. Figure 13 plots $E_c(k, \omega_p, y)$ of the different models at $kh = (2, 4)$. The error of the ν model is largest, and the errors for the W model and R_s^2 model are smaller. At the peak of the cross-spectral distributions ($|y/h| \approx 0.63$), the error of the R_s^2 model is smallest.

5. Conclusions and remarks

A composite sweeping-enhanced resolvent is developed in the present paper to predict the frequency spectra at a given wall-normal location and two-point cross-spectra of large-scale structures. The sweeping-enhanced resolvent is the standard resolvent operator augmented with eddy damping. The eddy damping can capture the decorrelation time scales of velocity fluctuations, whereas the eddy viscosity cannot represent the decorrelation process of velocity fluctuations. In the composite resolvents, the output of one resolvent is used as the input of another resolvent. In other words, a resolvent operator maps white-in-time random forcing to space–time coherent forcing, and then maps coherent forcing to the desired responses. Therefore, the composite resolvent avoids the incorrect prediction of the vanishing Taylor time microscales caused by white-in-time random forcing, and thus correctly reproduces the bandwidths of the frequency spectra at fixed wavenumbers.

The composite sweeping-enhanced resolvent (R_s^2 model) is evaluated in turbulent channel flows and compared with the standard resolvent (ν model) and the eddy-viscosity-enhanced resolvent (B model, W model and λ model). The main results are summarized as follows.

Figure 15. Frequency spectral distributions at (*a,c*) $kh = (1, 2)$ and (*b,d*) $kh = (4, 8)$ in the turbulent channel flows at $Re_\tau = 550$: (*a,b*) DNS results; (*c,d*) Results of the R_s^2 model.
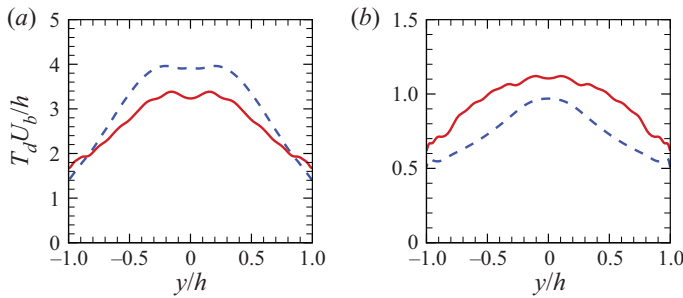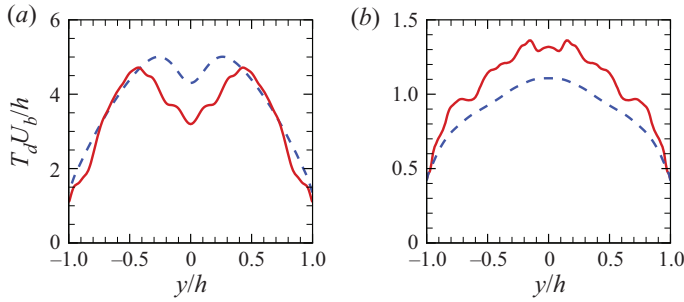

Figure 16. Comparison of the characteristic decay time scales obtained using the R_s^2 model with the DNS at (*a*) $kh = (1, 2)$ and (*b*) $kh = (4, 8)$ for $Re_\tau = 180$. Red solid lines: the DNS results. Blue dashed lines: the results of the R_s^2 model.

(i) The ν model can predict the peaks of the frequency spectra at a single wall-normal location, even though it treats the nonlinear forcing as white noise for simplicity. This is consistent with the previous results for the convection velocity in turbulent channel flows (Liu & Gayme 2020). However, the ν model underestimates the decay of time correlations, and the resultant characteristic time scales are substantially larger than the DNS results. Furthermore, the peaks of the two-point cross-spectra in the ν model are larger, and the cross-spectra decay faster than the DNS results.

(ii) The eddy-viscosity-enhanced models (B model and W model), particularly those with refined eddy viscosity and random forcing (λ model), improve the predictions on one-point frequency spectra, two-point cross-spectra and characteristic decay

Figure 17. Comparison of the characteristic decay time scales obtained using the R_s^2 model with the DNS at (a) $kh = (1, 2)$ and (b) $kh = (4, 8)$ for $Re_\tau = 550$. Red solid lines: the DNS results. Blue dashed lines: the results of the R_s^2 model.
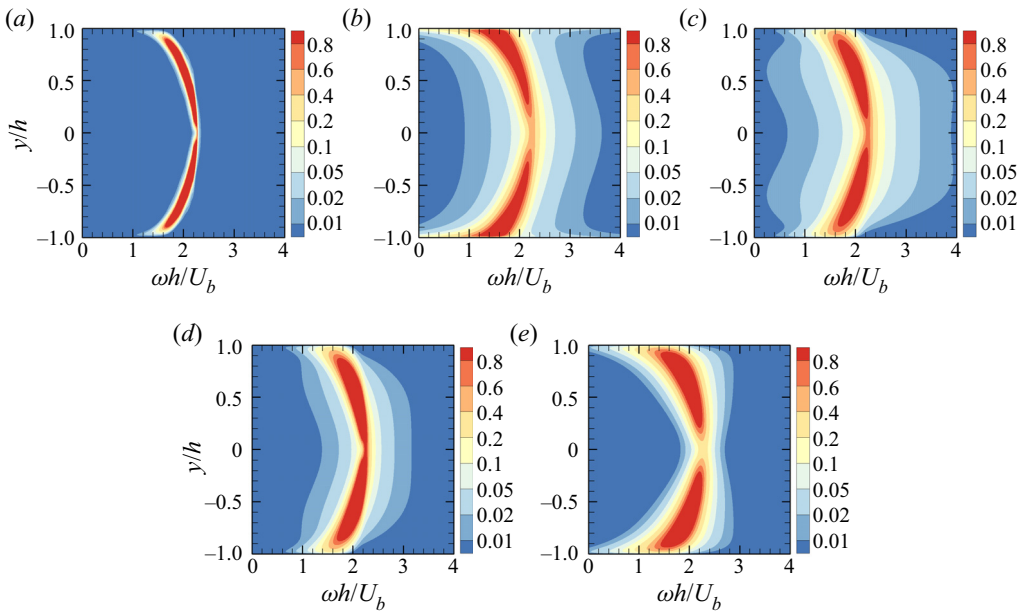

Figure 18. Frequency spectral distributions using the models at $kh = (2, 4)$ for large-scale structures at $Re_\tau = 1000$: (a) ν model, (b) B model, (c) W model, (d) λ model, (e) R_s^2 model.

time scales. However, as the wall distance increases, the characteristic decay time scales from the eddy-viscosity-enhanced models decrease over a large portion of the channel. This is in contrast to the DNS results, because the eddy viscosity is not designed to represent the decorrelation mechanism in turbulent channel flows.

(iii) The R_s^2 model can reproduce the features of the one-point frequency spectra and two-point cross-spectra, such as their peaks, areas and shapes. The characteristic decay time scales obtained from the R_s^2 model are in agreement with the DNS results. This is because eddy damping is introduced to represent the random sweeping decorrelation in turbulent channel flows, and the composite resolvent is introduced to avoid the direct action of white-in-time random forcing on the output velocities.
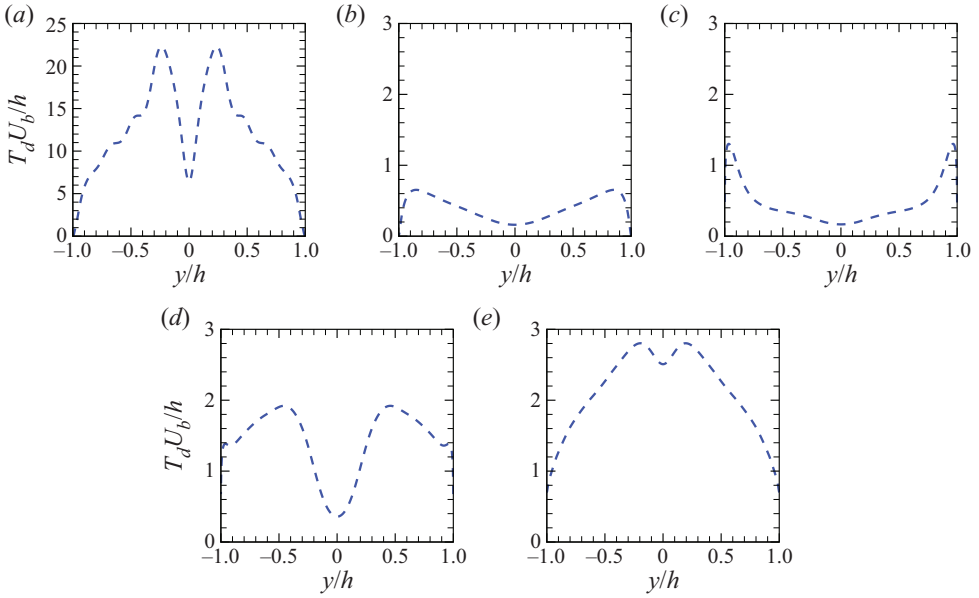
Figure 19. Characteristic decay time scales obtained using the models at $kh = (2, 4)$ for large-scale structures at $Re_\tau = 1000$: (*a*) ν model, (*b*) B model, (*c*) W model, (*d*) λ model, (*e*) R_s^2 model.
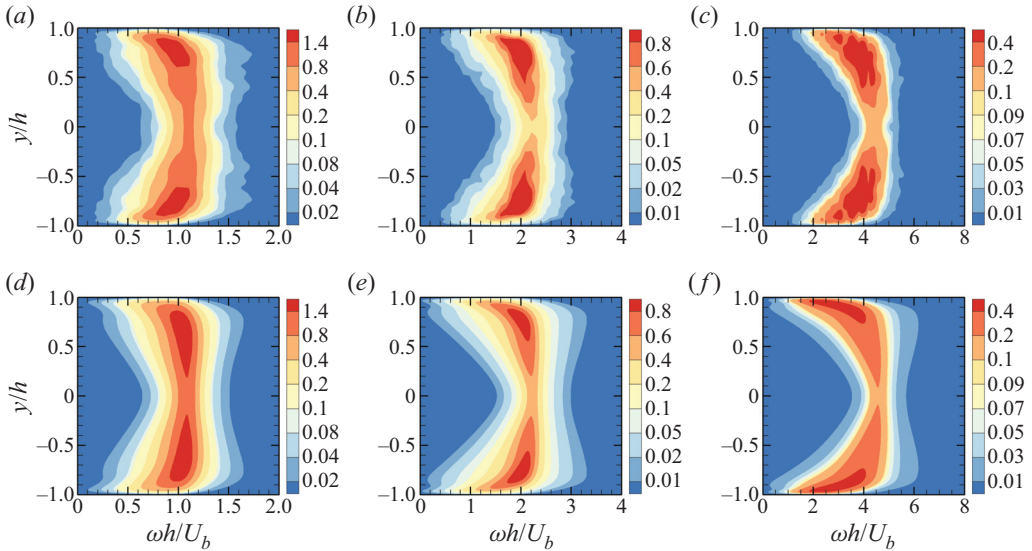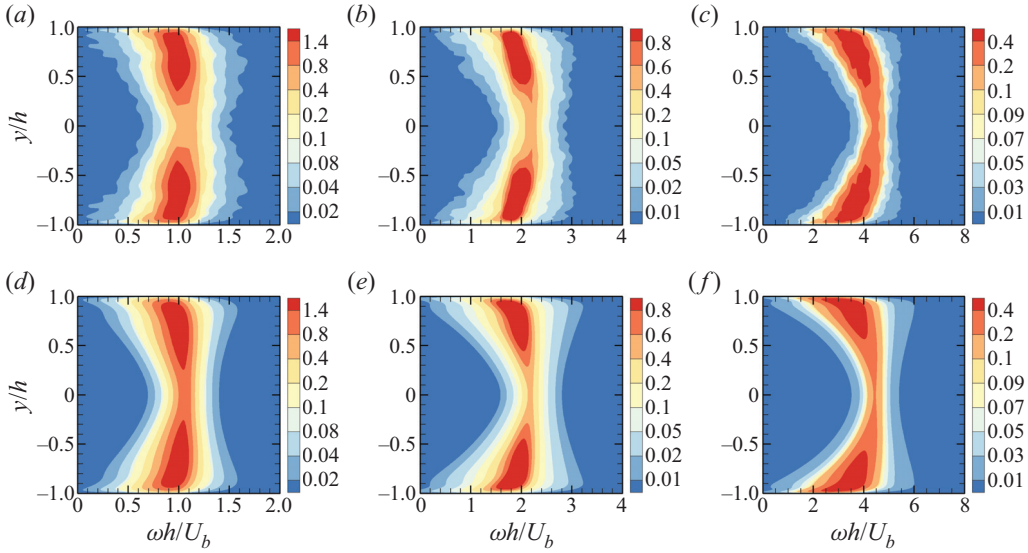

Figure 20. Frequency spectral distributions of the spanwise velocity fluctuations at $Re_\tau = 180$: (*a–c*) DNS results; (*d–f*) results of the R_s^2 model. Plots for (*a,d*) $kh = (1, 2)$, (*b,e*) $kh = (2, 4)$, (*c,f*) $kh = (4, 8)$.

Random sweeping decorrelation was originally proposed for homogeneous and isotropic turbulence (Kraichnan 1964; Tennekes 1975) and generalized to turbulent shear flows in physical space (He & Zhang 2006; Zhao & He 2009) and Fourier space (Wilczek, Stevens & Meneveau 2015*a*; Wilczek *et al.* 2015*b*). In the present work, eddy damping is introduced to represent the random sweeping decorrelation caused by nonlinear forcing in

956 A31-26

Figure 21. Frequency spectral distributions of the spanwise velocity fluctuations at $Re_\tau = 550$: $(a–c)$ DNS results; $(d–f)$ results of the $\mathbf{R}_s^2$ model. Plots for (a,d) $kh = (1, 2)$, (b,e) $kh = (2, 4)$, (c,f) $kh = (4, 8)$.
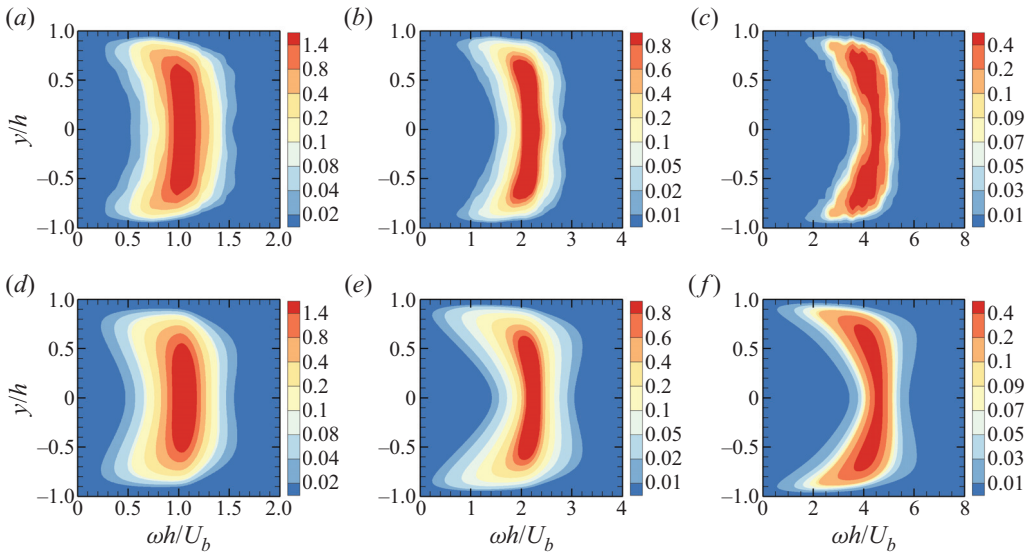

Figure 22. Frequency spectral distributions of the wall-normal velocity fluctuations at $Re_\tau = 180$: $(a–c)$ DNS results; $(d–f)$ results of the $\mathbf{R}_s^2$ model. Plots for (a,d) $kh = (1, 2)$, (b,e) $kh = (2, 4)$, (c,f) $kh = (4, 8)$.

the framework of the resolvent, while eddy viscosity is conventionally used to represent the energy dissipation caused by nonlinear forcing. In particular, sweeping velocities in the eddy-damping model are proposed and used to reproduce the frequency spectra.

The underlying mechanism of the $\mathbf{R}_s^2$ model for capturing the decorrelation time scales is as follows. (i) Composition of resolvents: one action of a resolvent on white-in-time random forcing yields vanishing Taylor time microscales of velocity fluctuations, while
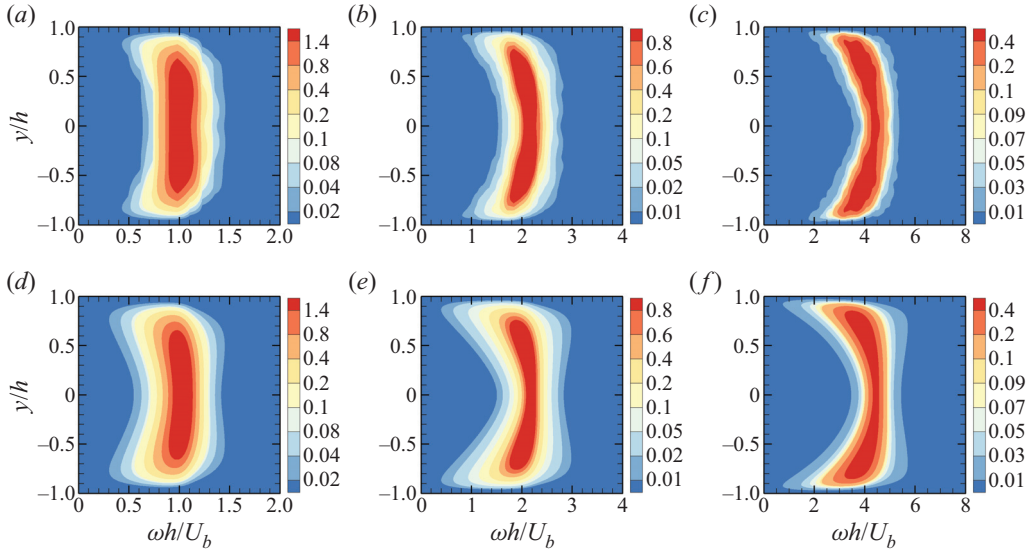
956 A31-27

Figure 23. Frequency spectral distributions of the wall-normal velocity fluctuations at $Re_\tau = 550$: $(a$–$c)$ DNS results; $(d$–$f)$ results of the R_s^2 model. Plots for (a,d) $kh = (1, 2)$, (b,e) $kh = (2, 4)$, (c,f) $kh = (4, 8)$.
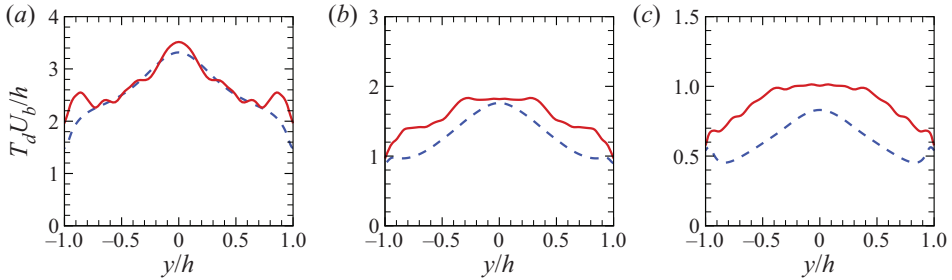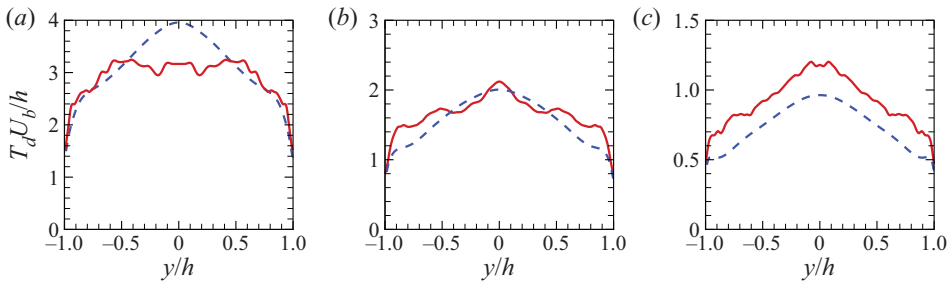

Figure 24. Comparison of the characteristic decay time scales of the spanwise velocity fluctuations obtained using the R_s^2 model with the DNS at $Re_\tau = 180$. Red solid lines, the DNS results; blue dashed lines, the results of the R_s^2 model. Plots for (a) $kh = (1, 2)$, (b) $kh = (2, 4)$, (c) $kh = (4, 8)$.

Figure 25. Comparison of the characteristic decay time scales of the spanwise velocity fluctuations obtained using the R_s^2 model with the DNS at $Re_\tau = 550$. Red solid lines, the DNS results; blue dashed lines, the results of the R_s^2 model. Plots for (a) $kh = (1, 2)$, (b) $kh = (2, 4)$, (c) $kh = (4, 8)$.
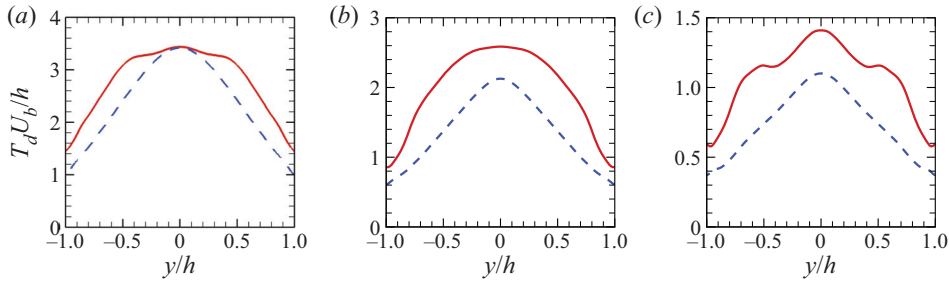
Figure 26. Comparison of the characteristic decay time scales of the wall-normal velocity fluctuations obtained using the R_s^2 model with the DNS at $Re_\tau = 180$. Red solid lines, the DNS results; blue dashed lines, the results of the R_s^2 model. Plots for (a) $kh = (1, 2)$, (b) $kh = (2, 4)$, (c) $kh = (4, 8)$.
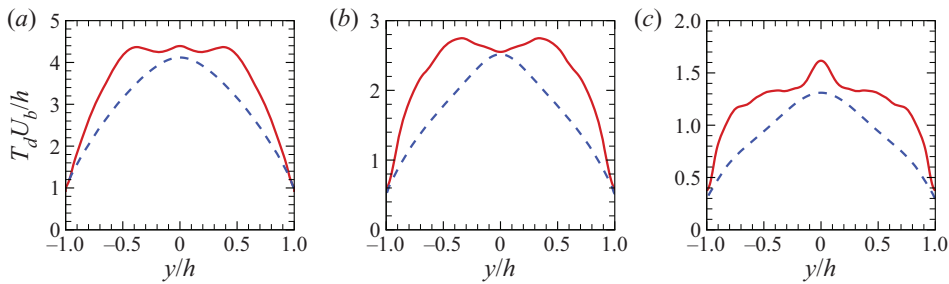

Figure 27. Comparison of the characteristic decay time scales of the wall-normal velocity fluctuations obtained using the R_s^2 model with the DNS at $Re_\tau = 550$. Red solid lines, the DNS results; blue dashed lines, the results of the R_s^2 model. Plots for (a) $kh = (1, 2)$, (b) $kh = (2, 4)$, (c) $kh = (4, 8)$.

two actions of the resolvent on white-in-time random forcing yield non-zero Taylor time microscales. (ii) Inclusion of the random sweeping effect: the random sweeping dominates the time decorrelation of velocity fluctuations in the logarithmic region (Zhao & He 2009; Wilczek *et al.* 2015*b*; Wu & He 2021*b*) and is taken into account by the R_s^2 model; the random sweeping cannot be represented by the eddy-viscosity-enhanced resolvent models.

Two-resolvent composition is used for predicting the frequency spectra of large-scale structures in turbulent channel flows. Multiple-resolvent composition can be constructed for a higher approximation, where either the sweeping-enhanced or the eddy-viscosity-enhanced resolvent is used. The multiple-resolvent composition can be considered as a deep resolvent that includes more desired physics. Planned future work will focus on the development of the multiple-resolvent composition to successive approximation to space–time statistics in turbulent flows, such as wall-bounded turbulence (Jiménez 2018; Wang, Wang & He 2018; Wang & Gao 2021), turbulent jets (Jordan & Colonius 2013; Schmidt *et al.* 2018) and wakes (De Cillis *et al.* 2022; Dong *et al.* 2022).

Declaration of interests. The authors report no conflict of interest.

Author ORCIDs.

Ⓓ Ting Wu https://orcid.org/0000-0002-7126-7883;

Ⓓ Guowei He https://orcid.org/0000-0003-4738-0816.

Appendix A. Frequency spectral distributions and characteristic decay time scales at $kh = (1, 2)$ and $kh = (4, 8)$

We calculate the frequency spectral distributions and the characteristic decay time scales at the wavenumber vectors $kh = (1, 2)$ and $kh = (4, 8)$ for large-scale structures. For $kh = (1, 2)$, the factor is $\beta(k) = 0.083$ at $Re_\tau = 180$, and $\beta(k) = 0.051$ at $Re_\tau = 550$. For $kh = (4, 8)$, the factor is $\beta(k) = 0.061$ at $Re_\tau = 180$, and $\beta(k) = 0.038$ at $Re_\tau = 550$.

Figures 14 and 15 plot the frequency spectral distributions at $kh = (1, 2)$ and $kh = (4, 8)$. The results show that the spectral distributions obtained using the R_s^2 model are consistent with the DNS results. Figures 16 and 17 compare the characteristic decay time scales from the R_s^2 model with the DNS results at $kh = (1, 2)$ and $kh = (4, 8)$. For $kh = (1, 2)$, the characteristic decay time scales from the R_s^2 model are slightly larger than those from the DNS. For $kh = (4, 8)$, the characteristic decay time scales for the R_s^2 model are slightly smaller than those from the DNS. Despite these slight differences, the wall-normal variation trends of the characteristic decay time scales from the R_s^2 model are consistent with the DNS results.

Appendix B. Frequency spectral distributions and characteristic decay time scales obtained using the resolvent-based models at $kh = (2, 4)$ for large-scale structures at $Re_\tau = 1000$

We calculate the frequency spectral distributions and characteristic decay time scales obtained using the resolvent-based models at $kh = (2, 4)$ for large-scale structures at $Re_\tau = 1000$, where the mean velocity and r.m.s. are from the DNS results of Lee & Moser (2015). In the R_s^2 model, $\beta(k)$ is taken as the same value at $Re_\tau = 550$, that is, $\beta(k) = 0.046$.

Figure 18 plots the frequency spectral distributions at $kh = (2, 4)$ for large-scale structures at $Re_\tau = 1000$. The results at this higher Reynolds number are similar to those at $Re_\tau = 180$ and 550. Figure 19 plots the characteristic decay time scales obtained by the models at $Re_\tau = 1000$. For a large region in the channel, as the wall distance increases, the characteristic decay time scales obtained by the B model and W model decrease. The characteristic time scales in the centre of the channel obtained by the λ model are less than those in the near-wall region. Similar to the results at $Re_\tau = 180$ and 550, the characteristic time scales in the centre of the channel from the R_s^2 model are larger than those in the near-wall region. The above observations at $Re_\tau = 1000$ are consistent with the results at $Re_\tau = 180$ and 550.

Geng *et al.* (2015) showed that in turbulent channel flows at $Re_\tau = 932$, Taylor's frozen-flow hypothesis becomes more applicable with increasing wall distance, implying that the characteristic decay time scales increase with increasing wall distance. This result implies that the R_s^2 model is still valid for the higher Reynolds number $Re_\tau = 1000$.

Appendix C. Frequency spectral distributions and characteristic decay time scales of the wall-normal and spanwise velocity fluctuations

Figures 20 and 21 plot the frequency spectral distributions of the spanwise velocity fluctuations. Figures 22 and 23 plot the frequency spectral distributions of the wall-normal velocity fluctuations. For the wall-normal and spanwise velocity fluctuations, the frequency spectral distributions from the R_s^2 model are consistent with the DNS results.

956 A31-30

Figures 24 and 25 compare characteristic decay time scales of the spanwise velocity fluctuations from the R_s^2 model with the DNS results. Figures 26 and 27 compare characteristic decay time scales of the wall-normal velocity fluctuations for the R_s^2 model with the DNS results. For the wall-normal and spanwise velocity fluctuations, the wall-normal variation trends of characteristic decay time scales for the R_s^2 model are also consistent with the DNS results.

REFERENCES

BAMIEH, B. & DAHLEH, M. 2001 Energy amplification in channel flows with stochastic excitation. *Phys. Fluids* **13**, 3258–3269.

BOSSUYT, J., MENEVEAU, C. & MEYERS, J. 2017 Wind farm power fluctuations and spatial sampling of turbulent boundary layers. *J. Fluid Mech.* **823**, 329–344.

CESS, R.D. 1958 A survey of the literature on heat transfer in turbulent tube flow. *Tech. Rep.* Report 8-0529-R24. Westinghouse Research.

DE CILLIS, G., CHERUBINI, S., SEMERARO, O., LEONARDI, S. & DE PALMA, P. 2022 Stability and optimal forcing analysis of a wind turbine wake: comparison with POD. *Renew. Energy* **181**, 765–785.

DONG, G.D., LI, Z.B., QIN, J.H. & YANG, X.L. 2022 How far the wake of a wind farm can persist for? *Theor. Appl. Mech. Lett.* **12**, 100314.

FARRELL, B.F. & IOANNOU, P.J. 1993 Stochastic forcing of the linearized Navier–Stokes equations. *Phys. Fluids* A **5**, 2600–2609.

FARRELL, B.F. & IOANNOU, P.J. 1998 Perturbation structure and spectra in turbulent channel flow. *Theor. Comput. Fluid Dyn.* **11**, 237–250.

GENG, C.H., HE, G.W., WANG, Y.S., XU, C.X., LOZANO-DURÁN, A. & WALLACE, J.M. 2015 Taylor's hypothesis in turbulent channel flow considered using a transport equation analysis. *Phys. Fluids* **27**, 025111.

GUPTA, V., MADHUSUDANAN, A., WAN, M.P., ILLINGWORTH, S.J. & JUNIPER, M.P. 2021 Linear-model-based estimation in wall turbulence: improved stochastic forcing and eddy viscosity terms. *J. Fluid Mech.* **925**, A18.

HE, G.W., JIN, G.D. & YANG, Y. 2017 Space–time correlations and dynamic coupling in turbulent flows. *Annu. Rev. Fluid Mech.* **49**, 51–70.

HE, G.W., WANG, M. & LELE, S.K. 2004 On the computation of space–time correlations by large-eddy simulation. *Phys. Fluids* **16** (11), 3859–3867.

HE, G.W. & ZHANG, J.B. 2006 Elliptic model for space–time correlations in turbulent shear flows. *Phys. Rev.* E **73**, 055303(R).

HUANG, K.Y. & KATUL, G.G. 2022 Profiles of high-order moments of longitudinal velocity explained by the random sweeping decorrelation hypothesis. *Phys. Rev. Fluids* **7** (4), 044603.

HWANG, Y. & COSSU, C. 2010*a* Amplification of coherent streaks in the turbulent Couette flow: an input–output analysis at low Reynolds number. *J. Fluid Mech.* **643**, 333–348.

HWANG, Y. & COSSU, C. 2010*b* Linear non-normal energy amplification of harmonic and stochastic forcing in the turbulent channel flow. *J. Fluid Mech.* **664**, 51–73.

ILLINGWORTH, S.J., MONTY, J.P. & MARUSIC, I. 2018 Estimating large-scale structures in wall turbulence using linear models. *J. Fluid Mech.* **842**, 146–162.

JIMÉNEZ, J. 2018 Coherent structures in wall-bounded turbulence. *J. Fluid Mech.* **842**, P1.

JORDAN, P. & COLONIUS, T. 2013 Wave packets and turbulent jet noise. *Annu. Rev. Fluid Mech.* **45**, 173–195.

JOVANOVIĆ, M.R. 2021 From bypass transition to flow control and data-driven turbulence modeling: an input–output viewpoint. *Annu. Rev. Fluid Mech.* **53**, 311–345.

JOVANOVIĆ, M.R. & BAMIEH, B. 2005 Componentwise energy amplification in channel flows. *J. Fluid Mech.* **534**, 145–183.

KARBAN, U., MARTINI, E., CAVALIERI, A.V.G., LESSHAFFT, L. & JORDAN, P. 2022 Self-similar mechanisms in wall turbulence studied using resolvent analysis. *J. Fluid Mech.* **939**, A36.

KATUL, G.G., BANERJEE, T., CAVA, D., GERMANO, M. & PORPORATO, A. 2016 Generalized logarithmic scaling for high-order moments of the longitudinal velocity component explained by the random sweeping decorrelation hypothesis. *Phys. Fluids* **28** (9), 095104.

KIM, K.C. & ADRIAN, R.J. 1999 Very large-scale motion in the outer layer. *Phys. Fluids* **11** (2), 417–422.

KRAICHNAN, R.H. 1964 Kolmogorov's hypotheses and Eulerian turbulence theory. *Phys. Fluids* **7**, 1723–1734.

LEE, M. & MOSER, R.D. 2015 Direct numerical simulation of turbulent channel flow up to $Re_\tau \approx 5200$. *J. Fluid Mech.* **774**, 395–415.

LESSHAFFT, L., SEMERARO, O., JAUNET, V., CAVALIERI, A.V.G. & JORDAN, P. 2019 Resolvent-based modeling of coherent wave packets in a turbulent jet. *Phys. Rev. Fluids* **4**, 063901.

LIU, C. & GAYME, D.F. 2020 An input–output based analysis of convective velocity in turbulent channels. *J. Fluid Mech.* **888**, A32.

MARTINI, E., CAVALIERI, A.V.G., JORDAN, P., TOWNE, A. & LESSHAFFT, L. 2020 Resolvent-based optimal estimation of transitional and turbulent flows. *J. Fluid Mech.* **900**, A2.

MCKEON, B.J. 2017 The engine behind (wall) turbulence: perspectives on scale interactions. *J. Fluid Mech.* **817**, P1.

MCKEON, B.J. & SHARMA, A.S. 2010 A critical-layer framework for turbulent pipe flow. *J. Fluid Mech.* **658**, 336–382.

MCMULLEN, R.M., ROSENBERG, K. & MCKEON, B.J. 2020 Interaction of forced Orr–Sommerfeld and Squire modes in a low-order representation of turbulent channel flow. *Phys. Rev. Fluids* **5** (8), 084607.

MOARREF, R. & JOVANOVIĆ, M.R. 2012 Model-based design of transverse wall oscillations for turbulent drag reduction. *J. Fluid Mech.* **707**, 205–240.

MOARREF, R., JOVANOVIĆ, M.R., TROPP, J.A., SHARMA, A.S. & MCKEON, B.J. 2014 A low-order decomposition of turbulent channel flow via resolvent analysis and convex optimization. *Phys. Fluids* **26** (5), 051701.

MORRA, P., NOGUEIRA, P.A.S., CAVALIERI, A.V.G. & HENNINGSON, D.S. 2021 The colour of forcing statistics in resolvent analyses of turbulent channel flows. *J. Fluid Mech.* **907**, A24.

MORRA, P., SEMERARO, O., HENNINGSON, D.S. & COSSU, C. 2019 On the relevance of Reynolds stresses in resolvent analyses of turbulent wall-bounded flows. *J. Fluid Mech.* **867**, 969–984.

NOGUEIRA, P.A.S., MORRA, P., MARTINI, E., CAVALIERI, A.V.G. & HENNINGSON, D.S. 2021 Forcing statistics in resolvent analysis: application in minimal turbulent Couette flow. *J. Fluid Mech.* **908**, A32.

PICKERING, E., RIGAS, G., SCHMIDT, O.T., SIPP, D. & COLONIUS, T. 2021 Optimal eddy viscosity for resolvent-based models of coherent structures in turbulent jets. *J. Fluid Mech.* **917**, A29.

PRASKOVSKY, A.A., GLEDZER, E.B., KARYAKIN, M.Y. & ZHOU, Y. 1993 The sweeping decorrelation hypothesis and energy-inertial scale interaction in high Reynolds number flows. *J. Fluid Mech.* **248**, 493–511.

RAN, W., ZARE, A. & JOVANOVIĆ, M.R. 2021 Model-based design of riblets for turbulent drag reduction. *J. Fluid Mech.* **906**, A7.

REYNOLDS, W.C. & HUSSAIN, A.K.M.F. 1972 The mechanics of an organized wave in turbulent shear flow. Part 3. Theoretical models and comparisons with experiments. *J. Fluid Mech.* **54** (2), 263–288.

ROSENBERG, K., SYMON, S. & MCKEON, B.J. 2019 Role of parasitic modes in nonlinear closure via the resolvent feedback loop. *Phys. Rev. Fluids* **4** (5), 052601.

RUBINSTEIN, R. & ZHOU, Y. 1999 Effects of helicity on Lagrangian and Eulerian time correlations in turbulence. *Phys. Fluids* **11** (8), 2288–2290.

RUBINSTEIN, R. & ZHOU, Y. 2000 The frequency spectrum of sound radiated by isotropic turbulence. *Phys. Lett.* A **267**, 379–383.

SCHMIDT, O.T., TOWNE, A., RIGAS, G., COLONIUS, T. & BRÈS, G.A. 2018 Spectral analysis of jet turbulence. *J. Fluid Mech.* **855**, 953–982.

SEMERARO, O., JAUNET, V., JORDAN, P., CAVALIERI, A.V.G. & LESSHAFFT, L. 2016 Stochastic and harmonic optimal forcing in subsonic jets. In *22nd AIAA/CEAS Aeroacoustics Conference, Lyon, France*, p. 2935. American Institute of Aeronautics and Astronautics (AIAA).

SLAMA, M., LEBLOND, C. & SAGAUT, P. 2018 A Kriging-based elliptic extended anisotropic model for the turbulent boundary layer wall pressure spectrum. *J. Fluid Mech.* **840**, 25–55.

SMITS, A.J., MCKEON, B.J. & MARUSIC, I. 2011 High-Reynolds number wall turbulence. *Annu. Rev. Fluid Mech.* **43**, 353–375.

SYMON, S., ILLINGWORTH, S.J. & MARUSIC, I. 2021 Energy transfer in turbulent channel flows and implications for resolvent modelling. *J. Fluid Mech.* **911**, A3.

TENNEKES, H. 1975 Eulerian and Lagrangian time microscales in isotropic turbulence. *J. Fluid Mech.* **67**, 561–567.

TOWNE, A., BRÈS, G.A. & LELE, S.K. 2017 A statistical jet-noise model based on the resolvent framework. In *23rd AIAA/CEAS Aeroacoustics Conference, Denver, CO, USA*, p. 3706. American Institute of Aeronautics and Astronautics (AIAA).

TOWNE, A., LOZANO-DURÁN, A. & YANG, X. 2020 Resolvent-based estimation of space–time flow statistics. *J. Fluid Mech.* **883**, A17.

VAN ATTA, C.W. & WYNGAARD, J.C. 1975 On higher-order spectra of turbulence. *J. Fluid Mech.* **72** (4), 673–694.

WANG, H.P. & GAO, Q. 2021 A study of inner–outer interactions in turbulent channel flows by interactive POD. *Theor. Appl. Mech. Lett.* **11** (1), 100222.

WANG, H.P., WANG, S.Z. & HE, G.W. 2018 The spanwise spectra in wall-bounded turbulence. *Acta Mechanica Sin.* **34** (3), 452–461.

WILCZEK, M. & NARITA, Y. 2012 Wave-number–frequency spectrum for turbulence from a random sweeping hypothesis with mean flow. *Phys. Rev.* E **86**, 066308.

WILCZEK, M., STEVENS, R.J.A.M. & MENEVEAU, C. 2015a Height-dependence of spatio-temporal spectra of wall-bounded turbulence – LES results and model predictions. *J. Turbul.* **16** (10), 937–949.

WILCZEK, M., STEVENS, R.J.A.M. & MENEVEAU, C. 2015b Spatio-temporal spectra in the logarithmic layer of wall turbulence: large-eddy simulations and simple models. *J. Fluid Mech.* **769**, R1.

WU, T., GENG, C.H., YAO, Y.C., XU, C.X. & HE, G.W. 2017 Characteristics of space–time energy spectra in turbulent channel flows. *Phys. Rev. Fluids* **2** (8), 084609.

WU, T. & HE, G.W. 2020 Local modulated wave model for the reconstruction of space–time energy spectra in turbulent flows. *J. Fluid Mech.* **886**, A11.

WU, T. & HE, G.W. 2021a Space–time energy spectra in turbulent shear flows. *Phys. Rev. Fluids* **6** (10), 100504.

WU, T. & HE, G.W. 2021b Stochastic dynamical model for space–time energy spectra in turbulent shear flows. *Phys. Rev. Fluids* **6**, 054602.

YANG, B.W., JIN, G.D., WU, T., YANG, Z.X. & HE, G.W. 2020 Numerical implementation and evaluation of resolvent-based estimation for space–time energy spectra in turbulent channel flows. *Acta Mechanica Sin.* **36** (4), 775–788.

ZARE, A., GEORGIOU, T.T. & JOVANOVIĆ, M.R. 2020 Stochastic dynamical modeling of turbulent flows. *Annu. Rev. Control Robot. Auton. Syst.* **3**, 195–219.

ZARE, A., JOVANOVIĆ, M.R. & GEORGIOU, T.T. 2017 Colour of turbulence. *J. Fluid Mech.* **812**, 636–680.

ZHAO, X. & HE, G.W. 2009 Space–time correlations of fluctuating velocities in turbulent shear flows. *Phys. Rev.* E **79**, 046316.